Honda Research Institute EU
Honda Research Institute Europe GmbH
https://www.honda-ri.de/

Benchmarking half-cell model fitting approaches for lithium-ion battery degradation diagnostics

Tingkai Li, Yifan Zhang, Benjamin Nowacki, Sina Navidi, Thomas Schmitt, Shan Hu, Chao Hu

2026

Preprint:

Copyright Elsevier 2026. This manuscript version is made available under the CC-BY-NC-ND 4.0 license http://creativecommons.org/licenses/by-nc-nd/4.0/

eTransportation 29 (2026) 100593

Contents lists available at ScienceDirect

eTransportation

journal homepage: www.journals.elsevier.com/etransportation

Benchmarking half-cell model fitting approaches for lithium-ion battery degradation diagnostics

Tingkai Li [a], Yifan Zhang [b], Benjamin Nowacki [a], Sina Navidi [a], Thomas Schmitt [c,d], Shan Hu [b], Chao Hu [a,*]

[a] School of Mechanical, Aerospace, and Manufacturing Engineering, University of Connecticut, Storrs, CT, 06269, USA
[b] Department of Mechanical Engineering, Iowa State University, Ames, IA, 50011, USA
[c] Honda Research Institute Europe GmbH, D-63073 Offenbach, Germany
[d] Zenules GmbH, D-64283 Darmstadt, Germany

ARTICLE INFO

Dataset link: https://digitalcommons.lib.uconn.edu/reil_datasets/6/, https://github.com/REIL-UConn/Multi-Objective-Optimization-for-Lithium-Ion-Battery-Degradation-Diagnostics

Keywords:
Lithium-ion batteries
Degradation diagnostics
Half-cell model fitting
Benchmarking

ABSTRACT

Accurate degradation diagnostics for lithium-ion batteries—specifically quantifying loss of active material on the positive and negative electrodes and loss of lithium inventory—enables component-level insights to improve design, control, and maintenance strategies. Among the few non-intrusive techniques, empirical half-cell model fitting to full-cell cycling data offers a promising path but often suffers from inconsistent fitting performance. To address this limitation, this work introduces a multi-objective optimization framework that enhances half-cell model fitting performance by jointly optimizing four degradation-aware objectives, which also serve as the goodness-of-fit metrics. Benchmarking studies on two datasets with distinct cell chemistries (LFP/Gr and LCO/Gr) and degradation pathways (fabricated capacity imbalance vs. cycling-induced aging) demonstrate improved alignment of phase changes and electrochemical-related signatures on differential voltage (dV/dQ) curves compared to conventional single-objective fitting. Built upon the successful benchmarking results, we present best practices and practical guidelines for implementing the proposed framework, including recommendations on half-cell fabrication and model formulation for broader application in degradation diagnostics.

1. Introduction

Lithium-ion batteries have been utilized for electrifying a range of applications, from delicate implantable medical devices to sophisticated electric vehicles. State estimation, including state of health (SOH) and state of charge (SOC), is essential to ensuring reliability and maintaining system performance over a battery's lifetime. Over the past decade, researchers have developed numerous approaches to achieve accurate state estimations, particularly with a focus on SOH estimation, as it directly reflects a battery's ability to store and deliver energy over its lifespan [1]. These methods can be broadly categorized into: physics-based, empirical-based, and data-driven approaches. Physics-based approaches typically employ mechanistic models such as single particle and pseudo-two-dimensional models, along with state observers like Kalman or particle filters to estimate internal states from external measurements [2–4]. While these methods offer strong physical interpretability and extrapolation potential, they are often challenging to parameterize because many parameters are not experimentally measurable, and usually require reasonable guesses based on deep domain knowledge, various characterization techniques, and time-consuming trial-and-error [5]. Empirical-based approaches instead fit experimental or in-field data to simplified algebraic or equivalent circuit models, enabling easier implementation at the cost of physical insight [6–8]. More recently, data-driven methods have gained traction by leveraging machine learning to map voltage, current, or impedance responses directly to health indicators [9–14]. For example, Shen et al. utilized partial segments of in-use charging data to estimate SOH via deep convolutional neural networks [9], while Nowacki et al. leveraged voltage responses from 100-second current pulse sequences as the input to multi-layer perceptron networks for rapid SOH estimation [12,13]. Although these methods achieve high accuracy, they offer limited mechanistic insight for design, control, or maintenance decisions [15–17].

Degradation diagnostics provide systematic tools for estimating component-level states, enabling identification of performance decline and guiding targeted design improvements. Degradation mechanisms — such as electrode particle cracking, loss of electric contact, lithium

* Corresponding author.
E-mail address: chao.hu@uconn.edu (C. Hu).

https://doi.org/10.1016/j.etran.2026.100593
Received 19 December 2025; Received in revised form 27 March 2026; Accepted 20 April 2026
Available online 7 May 2026
2590-1168/© 2026 Elsevier B.V. All rights are reserved, including those for text and data mining, AI training, and similar technologies.

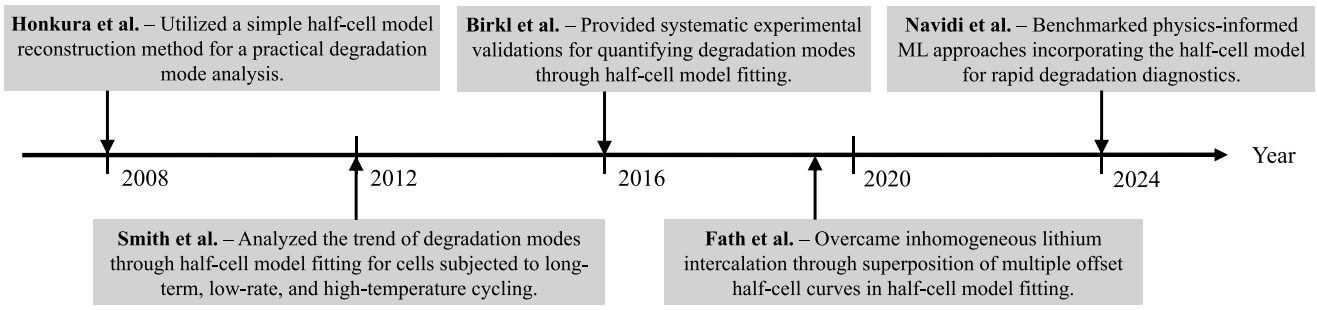

Fig. 1. Timeline of selected publications utilizing half-cell model fitting for degradation diagnostics [15,24,25,29,32]. The literature listed in this figure is not comprehensive and only serves as an informative summary.

plating, solid-electrolyte interphase (SEI) growth and decomposition — arise from interacting mechanical and electrochemical processes influenced by operating conditions (e.g., cumulative cycle number, total cycling time, ambient temperature, current loads, SOC levels) whose individual effects are difficult to isolate experimentally [15]. As a result, researchers commonly describe degradation in terms of three dominant modes observable through open circuit voltage (OCV) behavior: loss of active material in positive and negative electrodes (LAM_{PE} and LAM_{NE}, respectively) and loss of lithium inventory (LLI) [15,18].

Incremental capacity and differential voltage analyses have been widely employed to quantify these degradation modes by tracking shifts in peak locations and magnitudes, which correspond to electrode phase transitions [18–21]. As cells age, these peaks often tend to merge or disappear, complicating peak identifications and degrading diagnostic reliability [22,23]. To overcome these limitations, researchers have increasingly adopted half-cell models, which reconstruct the full-cell OCV curves as the superposition of positive and negative electrode half-cell OCV curves [15,22,24–37]. The quantification is achieved via curve fitting and by comparing the parameter values at an aged state with those at the pristine state. Parameterization strategies for half-cell models vary in complexity. One way to construct half-cell models is to superimpose half-cell pOCV curves measured from fabricated half-cells for the two electrodes [15,22,24–26,30–32]. Although the measured half-cell pOCVs are used in these works, the parameterization could differ. For instance, Birkl et al. used a six-parameter, two-step fitting scheme [26], whereas Lui et al. implemented a simpler four-parameter formulation [22]. The other approach is to simulate the half-cell pOCV using analytical formulations, such as multi-species multi-reaction (MSMR) models [33,34], single-particle models [35,38,39], or pseudo two-dimensional models [40]. Additional works also evaluate the possibility of fitting the half-cell model to cells with heterogeneous lithium intercalation by superposing multiple offset half-cell pOCVs [32] or by parameterizing analytical half-cell models [34]. However, the quality of individual fitting heavily depends on the quality of measurements, as it requires data from extremely slow-rate cycles with a low noise-to-signal ratio. Thus, when it comes to online estimation, pure curve-fitting methods can yield unreliable results at large-scale deployment of algorithms without domain expert supervision. Also, deploying curve-fitting or optimization algorithms for edge computation in battery management systems is a major challenge. To tackle this challenge and streamline online estimation, researchers explored physics-informed machine learning approaches, incorporating half-cell modeling with different machine learning algorithms, for fast and reliable online degradation diagnostics [27–29]. A brief timeline in Fig. 1 summarizes key literature on degradation diagnostics via half-cell model fitting. Please note that the literature highlighted in this figure is by no means inclusive, nor guaranteed to be the first work of the specific application or finding.

Nevertheless, key gaps remain. First, to the best of our knowledge, there is no established best practice for applying half-cell model-based degradation diagnostics in practical settings. The pioneering work by Birkl et al. provided a thorough theoretical support for degradation mode quantification using a half-cell model, but it lacked systematic benchmarking or implementation guidelines for half-cell model fitting [15]. Other works have utilized this method to solve various research problems, such as quick online estimation [29], generating labels for remaining useful life prediction [22,30], comparing different cell designs [25], or monitoring battery manufacturing process [37], rather than focusing on the method itself. Second, most recent implementations use a single-objective optimization for the fitting process. Although there are different objectives for curve fitting based on pOCV curves and differential voltage (dV/dQ) curves, they were either combined into a single objective via a weighted sum or downselected to a single objective for use. The simplest cases include the overall error of the pOCV curves only [15,25,30], the dV/dQ curves only [31], or the combination of the overall errors of pOCV and dV/dQ curves [33,34,37]. More advanced objectives are used, such as the peaks on dV/dQ [32,36] or multiple-windowed dV/dQ curves [32], along with the overall error of pOCV curves. All these objectives are meaningful for aligning the curves generated by the half-cell model, but the contribution of each to the overall fitting performance remains unclear. Also, researchers identified challenges in using single-objective optimization for automatic half-cell model fitting, especially the high run-to-run variations in fitted parameters on a multi-year aging dataset, which pose difficulties for direct implementation [22,29]. To ensure compliance with phase change and other physics-based characteristics, these researchers have resorted to an alternative—a human-intensive manual fitting procedure, which allows much better alignments of peaks in dV/dQ curves.

To address these gaps, this work introduces a multi-objective optimization framework for half-cell model fitting, incorporating four complementary, electrochemically motivated objectives that jointly improve goodness-of-fit and degradation relevance. The main contributions are as follows:

- Defines four standalone yet complementary objectives to better capture electrode phase transitions and degradation signatures during half-cell model fitting;
- Benchmarks different multi-objective optimization configurations on two datasets with distinct cell chemistries and degradation pathways;
- Consolidates best practices and implementation guidelines for researchers and practitioners implementing half-cell model fitting for degradation diagnostics.

The remainder of this article is organized as follows. Section 2 provides a detailed overview of the half-cell model and a step-by-step guide on reconstructing a full-cell OCV using the half-cell model. Section 3 describes the methodology for half-cell model fitting with multi-objective optimization. Section 4 presents the results of benchmarking studies on two datasets, followed by discussions on findings and general suggestions for a best practice. Section 5 concludes the paper.

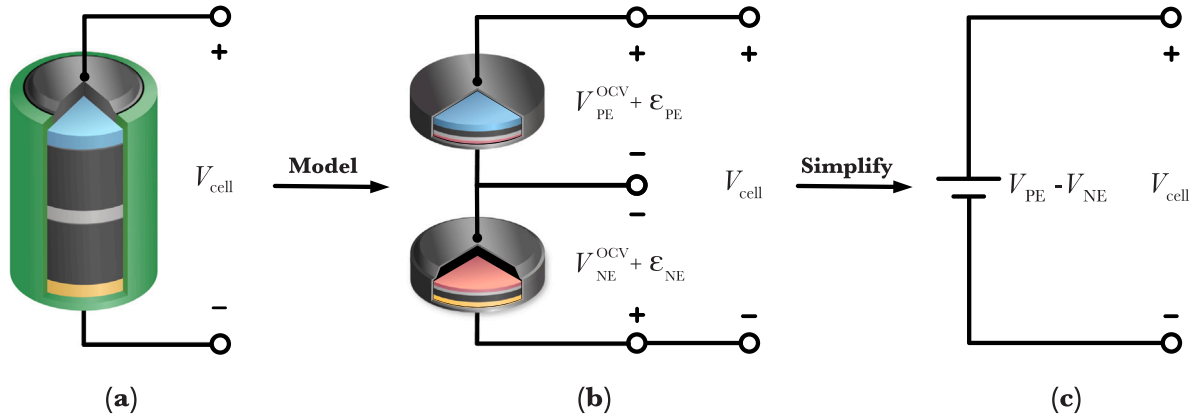

Fig. 2. Modeling the pOCV of a full-cell. (a) pOCV of the full-cell, (b) full-cell pOCV modeled from half-cell potentials, (c) a simplified equivalent circuit model of the full-cell.

2. Overview of the half-cell model

A half-cell model is an empirical, simplified model for reconstructing the full-cell OCV curve based on the potential responses of the positive and negative electrodes. Typical cell chemistries use lithium cobalt oxide (LCO), lithium nickel cobalt aluminum oxide (NCA), lithium nickel manganese cobalt oxide (NMC), or lithium iron phosphate (LFP) as the cathode active material, with graphite (Gr) serving as the anode active material [41]. The OCV is the potential difference between electrodes when no current flows and at the equilibrium state [26]. In evaluating full-cells, the OCV provides significant information for degradation diagnostics, including SOH estimation and degradation mode quantification. This stems from the fact that different degradation modes create unique OCV responses at different SOC levels [15,42,43]. Bringing a cell to different SOC levels requires charging or discharging between its full operating voltage range. However, the measured voltage response of a cell during cycling varies with charge or discharge currents due to underlying kinetic effects, such as mass transport resulting from ion migration and diffusion, as well as double-layer effects [44]. To eliminate these kinetic effects, a relaxation period is required such that cell voltage equilibrium is achieved before measurement. However, this approach may not be feasible due to the functional limitations of battery testers and/or other lab equipment. As an alternative, the pseudo-OCV (pOCV) is introduced to simplify the experiment. A pOCV curve refers to the potential versus capacity measurements taken with standard constant-current (CC) charging and discharging steps at a very slow rate (e.g., $I < C/30$), such that the underlying kinetic effects are negligible. For the rest of this paper, the methodology for half-cell modeling will be based on the pOCV curves. Additional information regarding the general experimental procedures for half-cell fabrication, either from pristine materials or recovered electrodes from commercial cells, and data collection can be found in Appendix A.1.

Once pOCV versus SOC measurements for both PE and NE half-cells (half-cell potential curves) are available, either from fabricated half-cells following Procedure A1 or from vendors, a half-cell model can be used to reconstruct pOCV responses of the full-cell at different SOCs. In this work, we focus on the half-cell model formulation based on the research from Honkura et al. [24]. Although general information for half-cell model implementation is provided in the following step-by-step procedure, more details about the model formulation, assumptions about unmodeled physics, and the physical meaning of each parameter can be found in the original paper [24]. As shown in Fig. 2(a–b), a full-cell can be modeled as two half-cells in series. During the charging, the PE half-cell represents the delithiation process, and the NE half-cell represents the lithiation process. The processes reverse during discharge. For the experimental half-cells, the measured pOCV potential contains two parts: the open-circuit electrode potential (V_{PE}^{OCV} and V_{NE}^{OCV}) and unmodeled physics (ε_{PE} and ε_{NE}), which can be expressed as

$$V_{PE} = V_{PE}^{OCV} + \varepsilon_{PE} \text{ and } V_{NE} = V_{NE}^{OCV} + \varepsilon_{NE}. \tag{1}$$

The unmodeled physics arises from various sources, such as overpotentials due to the aforementioned kinetic effects and the voltage drop due to internal ohmic resistances. Given that capturing every possible underlying physics is impossible, we can simplify the model by assuming that ε_{PE} and ε_{NE} are negligible as long as the half-cells are cycled at a very slow rate. Under this assumption, the full-cell voltage can be approximated by the potential difference between the PE and NE (Fig. 2(c)). Mathematically, the half-cell model for pOCV (V_{cell}) can be expressed as [24].

$$\begin{aligned} V_{cell} &= V_{PE} - V_{NE} \\ &= \left(V_{PE}^{OCV} + \varepsilon_{PE}\right) - \left(V_{NE}^{OCV} + \varepsilon_{NE}\right) \\ &\approx V_{PE}^{OCV} - V_{NE}^{OCV} \\ &\approx V_{cell}^{OCV}. \end{aligned} \tag{2}$$

To help visualize the process of developing a half-cell model as shown in Fig. 3, we utilize data from a sample LCO/graphite full-cell and its corresponding fabricated half-cells. A typical procedure to simulate a full-cell curve based on the half-cell model in Eq. (2) consists of the following five sequential steps.

- *Step 1: Obtain potential versus capacity data from half-cells*
  By following the fabrication and data collection procedures mentioned in Appendix A.1, we can obtain potential versus half-cell capacity responses for both the PE and NE, denoted as $V_{PE}^{hc}\left(Q_{PE}^{hc}\right)$ and $V_{NE}^{hc}\left(Q_{NE}^{hc}\right)$, where the superscript hc denotes that these are measurements from experimental half-cells.
- *Step 2: Calculate potential versus specific capacity curves*
  The measurements from the PE and NE half-cells under *Step 1* cannot be directly applied to a half-cell model and must be transformed with respect to capacity, either per area or gram of active mass. By doing so, the transformed curves can be easily scaled up to reflect full-cell-size electrodes by multiplying the corresponding properties (i. e., the actual area or active mass). In this study, the half-cell curves measured from experimental half-cells are normalized by the active mass values (m_{PE}^{hc} and m_{NE}^{hc}) to obtain curves in terms of the specific capacity (q_{PE} and q_{NE}). The specific capacities can be obtained as

$$q_{PE} = \frac{Q_{PE}^{hc}}{m_{PE}^{hc}} \text{ and } q_{NE} = \frac{Q_{NE}^{hc}}{m_{NE}^{hc}}. \tag{3}$$

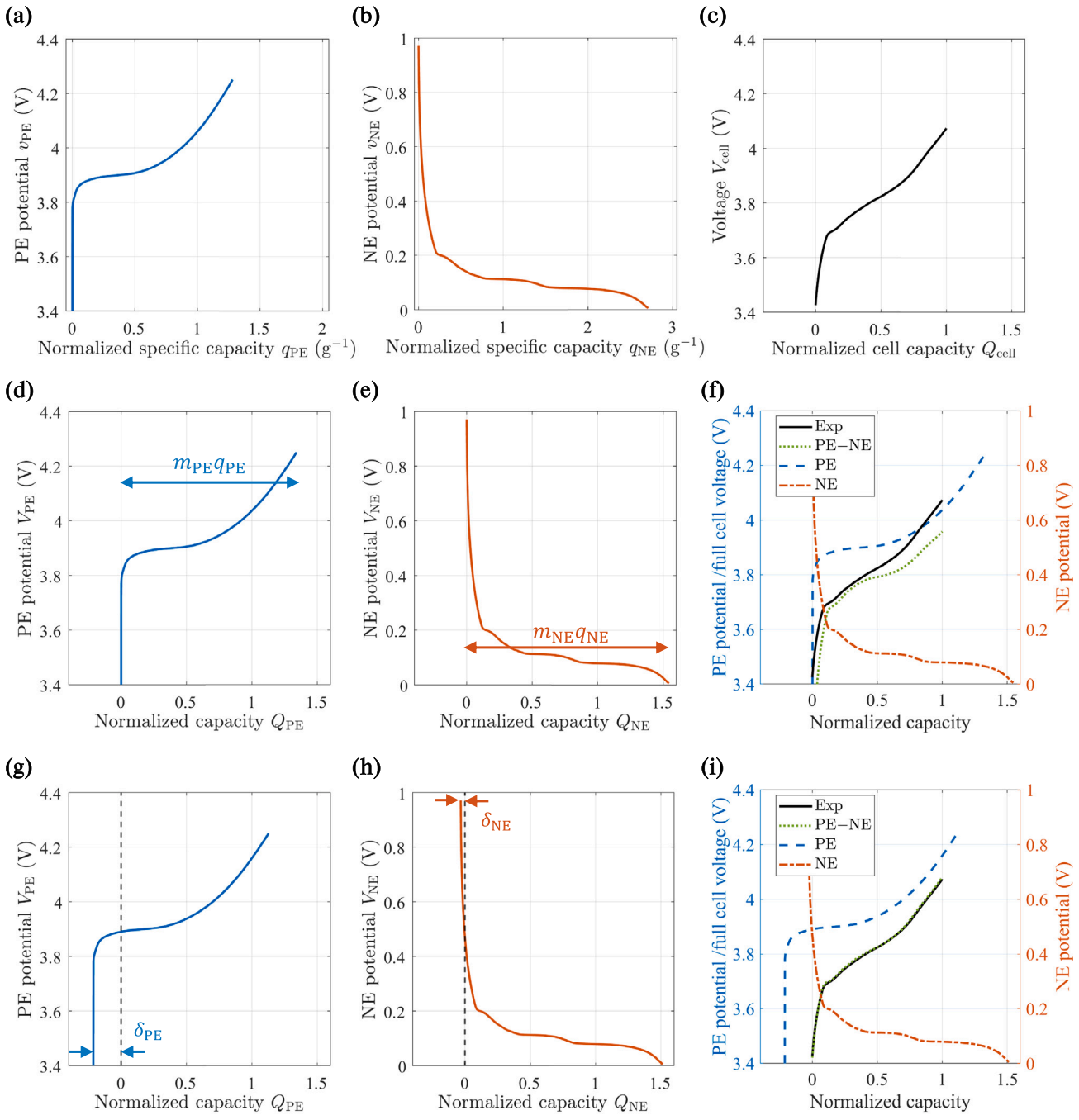

Fig. 3. Visualization of half-cell model construction. (a–b) Measured potential versus specific capacity of PE and NE (q_{PE} and q_{NE}), respectively; (c) measured full-cell capacity versus voltage from a sample cell; (d–e) scaled potential versus capacity of PE and NE by the active mass values of the sample cell, respectively; (f) superposition of (d) and (e); (g–h) shifted potential versus capacity of PE and NE from (d) and (e) by δ_{PE} and δ_{NE}, respectively; (i) superposition of (g) and (h). The capacity values in this set of figures are scaled by the capacity of a pristine full cell shown on (c).

The capacity potential curves in terms of the specific capacity (v_{PE} and v_{NE}), later referred to as specific voltage potential curves, are

$$v_{PE}\left(q_{PE}\right) = V_{PE}^{hc}(Q_{PE}^{hc})\Big|_{Q_{PE}^{hc}=q_{PE}m_{PE}^{hc}} \tag{4}$$

and

$$v_{NE}\left(q_{NE}\right) = V_{NE}^{hc}(Q_{NE}^{hc})\Big|_{Q_{NE}^{hc}=q_{NE}m_{NE}^{hc}}. \tag{5}$$

By performing the transformation, we assume that the obtained potential curves in terms of the specific capacity reflect the electrode material properties and are now independent of the size and form factor of experimental half-cells.

- *Step 3: Scale specific capacity potential curves to full-cell size electrodes* With the two specific capacity potential curves, as shown in Fig. 3(a–b), a half-cell model is built based on linear manipulations of these curves (i.e., multiplication, horizontal shifting, and superimposition). Fig. 3(c) shows a sample full-cell to which we are trying to fit the half-cell model. To obtain the potential versus capacity curves of full-cell electrodes, we must first obtain the values of active mass. If these values are unavailable from the vendors, they can be estimated empirically by subtracting the weight of the current collector from that of the whole electrode. Then, we can map the specific capacity to the full-cell capacity via multiplying the specific capacity values by the active masses of the full-cell

electrodes, as shown in the following equations:

$$V_{\mathrm{PE}}(Q_{\mathrm{PE}}) = v_{\mathrm{PE}}(q_{\mathrm{PE}})\big|_{q_{\mathrm{PE}}=\frac{Q_{\mathrm{PE}}}{m_{\mathrm{PE}}}} \text{ and } V_{\mathrm{NE}}(Q_{\mathrm{NE}}) = v_{\mathrm{NE}}(q_{\mathrm{NE}})\big|_{q_{\mathrm{NE}}=\frac{Q_{\mathrm{NE}}}{m_{\mathrm{NE}}}}. \tag{6}$$

These operations are visualized in Fig. 3(d–e). However, when we superimpose these two curves, Fig. 3(f) shows that the reconstructed curve does not match the full-cell QV curve. The reason is that when cells operate within the designed voltage range, both the PE and NE of cells are neither fully lithiated nor fully delithiated. Cell manufacturers intentionally do this to protect the electrodes from severe degradation.

- *Step 4: Add slippage parameters*
  For a given full-cell pOCV curve, the stoichiometry of each electrode at the beginning of the charge or discharge step is different from that of the half-cell curves, since the half-cell curves are measured independently and often aimed to cover the maximum possible range of stoichiometry during cycling. Therefore, to align the two half-cell curves with the full-cell curve, we need to shift them horizontally to account for the different starting stoichiometries. The shifting is achieved by introducing two slippage parameters δ_{PE} and δ_{NE} to align the starting stoichiometry of the half-cell curves with that of the full-cell curve. In theory, the half-cell model requires an additional set of parameters to define the end stoichiometry for each electrode. However, under an ideal assumption that the decrease in stoichiometry on one electrode equals the increase on the counter-electrode, the ending stoichiometry is fully constrained by the active mass of the electrode (which translates into the electrode capacity) and the full-cell voltage operating window. Fig. 3(g–h) demonstrates the potential curves after slippage parameters are applied to the curves shown in Fig. 3(d–e). By superimposing the two shifted curves, as illustrated in Fig. 3(i), the reconstructed pOCV overlays accurately with the sample measurement.
  The mathematical expression of pOCV from a fully-constructed half-model, in terms of two specific potential responses $\{v_{\mathrm{PE}}, v_{\mathrm{NE}}\}$ and four half-cell model parameters $\{m_{\mathrm{PE}}, m_{\mathrm{NE}}, \delta_{\mathrm{PE}}, \delta_{\mathrm{NE}}\}$, is shown as

$$\begin{aligned}\hat{V}_{\mathrm{cell}}(Q_{\mathrm{cell}}) &= V_{\mathrm{PE}}(Q_{\mathrm{cell}}) - V_{\mathrm{NE}}(Q_{\mathrm{cell}}) \\ &= v_{\mathrm{PE}}(q_{\mathrm{PE}})\big|_{q_{\mathrm{PE}}=\frac{Q_{\mathrm{cell}}-\delta_{PE}}{m_{\mathrm{PE}}}} - v_{\mathrm{NE}}(q_{\mathrm{NE}})\big|_{q_{\mathrm{NE}}=\frac{Q_{\mathrm{cell}}-\delta_{NE}}{m_{\mathrm{NE}}}} \\ &\text{with } V_{\min} \le \hat{V}_{\mathrm{cell}}(Q_{\mathrm{cell}}) \le V_{\max},\end{aligned} \tag{7}$$

  where $V_{\min}$ and $V_{\max}$ are the voltage limits of the full-cell operating window. Furthermore, by applying the chain rule, the differential voltage curve of a half-cell model is derived from Eq. (7) as

$$\begin{aligned}\frac{d\hat{V}_{\mathrm{cell}}}{dQ} &= \frac{dV_{\mathrm{PE}}}{dQ_{\mathrm{PE}}}(Q_{\mathrm{cell}}) - \frac{dV_{\mathrm{NE}}}{dQ_{\mathrm{NE}}}(Q_{\mathrm{cell}}) \\ &= \frac{1}{m_{\mathrm{PE}}}\frac{dv_{\mathrm{PE}}}{dq_{\mathrm{PE}}}(q_{\mathrm{PE}})\bigg|_{q_{\mathrm{PE}}=\frac{Q_{\mathrm{cell}}-\delta_{PE}}{m_{\mathrm{PE}}}} - \frac{1}{m_{\mathrm{NE}}}\frac{dv_{\mathrm{NE}}}{dq_{\mathrm{NE}}}(q_{\mathrm{NE}})\bigg|_{q_{\mathrm{NE}}=\frac{Q_{\mathrm{cell}}-\delta_{NE}}{m_{\mathrm{NE}}}}.\end{aligned} \tag{8}$$

  At this point, a half-cell model is fully defined and can be used to simulate pOCV curves of full-cells. Different sets of the four half-cell model parameters (m_{PE}, m_{NE}, δ_{PE}, and δ_{NE}) can be applied to the half-cell model to study the full-cell pOCV response under different active mass ratios and/or different levels of lithiation/delithiation at the start of cycling. However, if the half-cell model intends to help estimate the current SOH of a given full-cell, which is the main focus of this paper, the model will be fitted to a full-cell measurement. This fitting process determines the active masses and slippage parameters best describing the given full-cell. An additional step is thus needed to iteratively acquire the best fit.
- *Step 5: Adjust parameters to optimize the fitting*
  The four parameters that define the half-cell model, m_{PE}, m_{NE}, δ_{PE}, and δ_{NE}, can be tuned to obtain an optimal fit to the measured full-cell QV curve. This fitting process can be designed to minimize various evaluation criteria, which will be further discussed in Section 3.

There are open-source software available for half-cell modeling, such as the ‘alawa Toolbox from the University of Hawai‘i at Mānoa [18] and the PyBaMM library [39]. These tools allow battery engineers to quickly model the voltage response of cells at different aging states and cycling rates. More specifically, the ‘alawa Toolbox provides a well-designed user interface for simulating full-cell pOCV responses by varying parameters related to degradation across cycles, such as LAM, LLI, ohmic resistance, and kinetic effect. Also, this toolbox offers the option to simulate pOCV curves at various C-rates when the user provides CC cycling measurements across a wide range of C-rates for interpolation, or uses one of the built-in electrodes. On the other hand, the PyBaMM library focuses on physics-based half-cell modeling, meaning the half-cell pOCV curves are derived from reduced-order models, such as a single-particle model, which requires an extensive parameterization process known to be challenging [5]. These tools, for example, can synthesize a large amount of battery data in a short period of time by varying model parameters, which augments datasets for data-driven degradation diagnostics modeling and serves as a digital twin of batteries [45,46]. Although they are powerful for simulating the full-cell pOCV given the model parameters, they are not designed for backward fitting problems (estimating the parameters given full-cell measurements), which are addressed in this work.

3. Degradation diagnostics using a half-cell model

This section covers the process of utilizing the half-cell model to quantify the degradation modes of the Li-ion battery with different degradation paths and extents. We first introduce the four complementary objectives designed for fitting the half-cell model to a specific full-cell measurement, along with brief descriptions of multi-objective optimization algorithms used in this work. In addition, the three degradation parameters derived from the fitted half-cell model, each quantifying a specific degradation mode, are discussed.

3.1. Objectives for half-cell model fitting

Step 5 of Section 2 requires objective functions to find an optimally fitted half-cell model. The model fitting process identifies the optimal values of the half-cell model parameters given measurements from a full-cell. Note that the primary purpose of this step is not to use the half-cell model to simulate QV or dV/dQ curves, given a set of predefined half-cell model parameters, but rather to optimize the set of half-cell model parameters $\{m_{\mathrm{PE}}, m_{\mathrm{NE}}, \delta_{\mathrm{PE}}, \delta_{\mathrm{NE}}\}$ via a typically iterative process. We define four objectives (see Fig. 4) to measure the goodness of fit of the half-cell model with a given set of parameters, which can be used individually or in combination.

- *Objective 1: matching the endpoints of QV curves*
  The first objective measures the differences between the left and right endpoints of a simulated QV curve ($Q(V)$) and those from a measured QV curve. Minimizing these differences will ensure that the operating voltage range and total capacity simulated match those observed experimentally. Mathematically, this objective can be written as

$$\mathrm{MSE}_{\mathrm{end}} = \frac{1}{2}\left[\left(\hat{V}_{\mathrm{cell}}(Q_{\mathrm{cell}} = Q_{\min};\theta) - V_{\min}\right)^2 + \left(\hat{V}_{\mathrm{cell}}(Q_{\mathrm{cell}} = Q_{\max};\theta) - V_{\max}\right)^2\right], \tag{9}$$

  where $\theta = [m_{\mathrm{PE}}, m_{\mathrm{NE}}, \delta_{\mathrm{PE}}, \delta_{\mathrm{NE}}]^{\mathrm{T}}$, $V_{\min}$ and $V_{\max}$ are lower and upper voltage cutoffs of the measured full-cell QV curve, and $Q_{\min}$ and

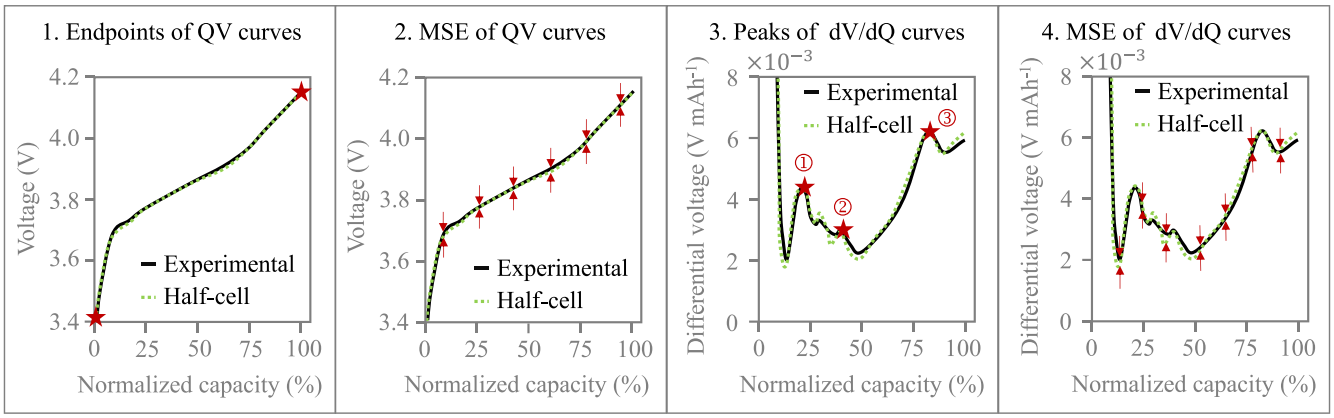

Fig. 4. Overview of four fundamental half-cell model fitting objectives.

Q_{max} are the corresponding capacity readings at the lower and upper voltage cutoffs, respectively.

- *Objective 2: minimizing the overall fitting error of QV curves*

The second objective examines the discrepancy between the model-simulated and measured full-cell voltages at each of a predefined set of capacity setpoints. This objective focuses on the overall goodness of fit between the QV curve simulated (reconstructed) by a half-cell model and a measured curve. In particular, the mean squared error (MSE) metric is used as it penalizes points with larger fitting errors during the minimization. This objective can be expressed as

$$\mathrm{MSE}_{\mathrm{QV}} = \frac{1}{N}\sum_{i=1}^{N}\left(\hat{V}_{\mathrm{cell}}(Q_i;\boldsymbol{\theta}) - V_{\mathrm{cell}}(Q_i)\right)^2, \tag{10}$$

where N represents the number of predefined equidistant capacity setpoints ($Q_{\mathrm{cell}} = \{Q_1, Q_2, \ldots, Q_N\}$), which can be obtained by interpolation.

- *Objective 3: matching the peaks of dV/dQ curves*

The third objective is to align the peaks of the reconstructed dV/dQ curve with those of the measured curve. Peak locations on the capacity axis and the corresponding peak areas (defined by height, width, and curvature) are associated with the phase changes occurring within electrodes during charging or discharging [47]. More specifically, the shift in peak locations reflects the change in the lithium stoichiometry of the electrodes during cycling caused by LLI, while the change in peak areas is dictated by the amount of active mass in the electrode that participates in the phase change reaction due to LAM. This objective constrains peak locations and areas during the fitting process, thus helping the half-cell model better reflect the underlying electrochemical dynamics. With phase changes during charging or discharging being cell-dependent (e.g., cell chemistry, predefined voltage cutoffs), we must first identify which of the major peaks should be evaluated with this objective. For example, for the LCO/Gr cell used in the benchmarking study in Section 4, we focus on matching the three peaks highlighted in Fig. 4. The formula for this objective is

$$\begin{aligned}\mathrm{MSE}_{\mathrm{peaks}} = \frac{1}{P}\sum_{i=1}^{P}\Bigg[&\left(\hat{Q}_{\mathrm{peak},i}(\boldsymbol{\theta}) - Q_{\mathrm{peak},i}\right)^2 \\ &+ \frac{1}{2a+1}\sum_{j=-a}^{a}\left(\frac{\widehat{dV}_{\mathrm{cell}}}{dQ}\left(Q_{\mathrm{cell}} = \hat{Q}_{\mathrm{peak},i} + j;\boldsymbol{\theta}\right)\right. \\ &\left.-\frac{dV_{\mathrm{cell}}}{dQ}\left(Q_{\mathrm{cell}} = Q_{\mathrm{peak},i} + j\right)\right)^2\Bigg],\end{aligned} \tag{11}$$

where P is the number of peaks identified for alignment evaluation, $Q_{\mathrm{peak},i}$ is the location of the i-th identified peak, and a is the number of discrete samples before and after a given peak for calculating the error between two dV/dQ curves. The first error term in Eq. (11) evaluates the difference between peak locations, and the second term evaluates the difference between magnitudes of predefined peak segments.

- *Objective 4: minimizing the overall fitting error of dV/dQ curves*

Similar to *Objective 2*, the fourth objective is to calculate the MSE, thus evaluating the discrepancy between a model-reconstructed differential voltage curve (dV/dQ) and a measured one, which can be expressed as

$$\mathrm{MSE}_{\mathrm{dV/dQ}} = \frac{1}{N}\sum_{i=1}^{N}\left(\frac{\widehat{dV}_{\mathrm{cell}}}{dQ}(Q_{\mathrm{cell}} = Q_i;\boldsymbol{\theta}) - \frac{dV_{\mathrm{cell}}}{dQ}(Q_{\mathrm{cell}} = Q_i)\right)^2. \tag{12}$$

However, dV/dQ curves usually exhibit high values at the low- and high-SOC regions, which could lead to unexpected bias toward those regions due to inevitable high residual values and the resulting distortion in calculating MSE. In subsequent implementations, data points exceeding a preset dV/dQ threshold are omitted from the calculation. This practice has been reported in the literature to be effective when considering $\mathrm{MSE}_{\mathrm{dV/dQ}}$ in half-cell model fitting [31,32].

With these four fundamental objectives, we can formulate the optimization problem to find the best set of half-cell model parameters given a cell measurement (QV and dV/dQ). However, each objective provides unique information during the fitting process and needs to be used jointly in most cases, which makes finding the best set of weights cell-specific and challenging. In this work, we focus on utilizing multi- or many-objective optimization approaches to identify sets of parameters on the Pareto fronts. Specifically, we use two variants of non-dominated sorting genetic algorithms (NSGA), where NSGA-II is for multi-objective problems (with two to three objectives) and NSGA-III is for many-objective problems (with all four objectives) [48,49].

These two algorithms share common concepts, such as non-dominated sorting, elitism for preserving high-quality solutions across generations, and evolutionary operators, making them suitable for exploring trade-offs in multi-objective spaces. While both aim to approximate the Pareto front with a diverse set of high-quality solutions, they differ in their approach to maintaining diversity. NSGA-II uses a crowding distance metric to ensure solution spread, which is effective for problems with a small number of objectives. However, as the dimension of the problem increases, more samples obtained through NSGA-II will be non-dominated, and these non-dominated samples are often widespread in the high-dimensional space, leaving less selection pressure on guiding the algorithm to converge to the Pareto front [50]. In contrast, NSGA-III employs reference points to guide the search process, enabling better distribution and scalability in

high-dimensional objective spaces. Specifically, solutions in the space are associated with the corresponding closest pre-selected reference direction (a vector connecting a pre-selected reference point and the origin of the high-dimensional space), and NSGA-III performs niching to select a subset of solutions in each reference direction, emphasizing diversity preservation [49,50]. This niche-guided searching based on reference directions also preserves the selection pressure as the optimization progresses. This distinction makes NSGA-III more suitable for many-objective problems, whereas NSGA-II remains efficient and robust for problems with fewer objectives. More details about these algorithms can be found in the original works [48,49]. To justify the use of NSGA-III in four-objective problems, a comparison study has been conducted, which is summarized in the Supplementary Material. In brief, by comparing two evaluation metrics for multi-objective optimization, namely hypervolume and inverted generational distance plus, it is clear that NSGA-III outperforms NSGA-II in terms of both better convergence and lower run-to-run variations. On top of utilizing multi-objective optimization, since most of the recent works only used a single objective [15,30], which is the overall fitting error of QV curves (i.e., $\mathrm{MSE_{QV}}$), we also include such a single-objective case as the baseline for our benchmarking, and the ordinary genetic algorithm is used to perform this optimization. All the optimization in this work is completed with the pymoo package [51].

3.2. Degradation mode quantification

We need to define three degradation parameters to quantify the three major degradation modes ($\mathrm{LAM_{PE}}$, $\mathrm{LAM_{NE}}$, and LLI). In general, the loss of active masses during cycling can be at either the lithiated or delithiated state, and it is nearly impossible to trace the loss from both states. To simplify the diagnostics, we only consider the loss of active masses at the delithiated state, denoted as LAM, and that at the lithiated state can be represented by a combination of LAM and LLI [15]. In Section 2, we describe the process of utilizing a half-cell model to reconstruct the QV and dV/dQ curves for a given measurement from a cell. By fitting a half-cell model, we can directly quantify the loss of active materials on both electrodes, $\mathrm{LAM_{PE}}$ and $\mathrm{LAM_{NE}}$, by tracking the change of active masses (i.e., m_{PE} and m_{NE}) , which can be expressed as

$$\mathrm{LAM_{PE}} = \frac{m_{\mathrm{PE}}^{\mathrm{fresh}} - m_{\mathrm{PE}}}{m_{\mathrm{PE}}^{\mathrm{fresh}}} \text{ and } \mathrm{LAM_{NE}} = \frac{m_{\mathrm{NE}}^{\mathrm{fresh}} - m_{\mathrm{NE}}}{m_{\mathrm{NE}}^{\mathrm{fresh}}}, \tag{13}$$

where $m_{\mathrm{PE}}^{\mathrm{fresh}}$ and $m_{\mathrm{NE}}^{\mathrm{fresh}}$ are the active mass values for the cells at the fresh state. Although we use the change in the active mass m_{PE} and m_{NE} to track $\mathrm{LAM_{PE}}$ and $\mathrm{LAM_{NE}}$, respectively, the active mass values can be easily mapped to the remaining electrode capacity ($Q_{\mathrm{PE}}^{\max}$ and $Q_{\mathrm{NE}}^{\max}$) simply by multiplying them by the corresponding nominal electrode mass-specific capacity in the unit of Ah/g (i.e., $Q_{\mathrm{PE}}^{\max} = m_{\mathrm{PE}} q_{\mathrm{PE}}^{\max}$ and $Q_{\mathrm{NE}}^{\max} = m_{\mathrm{NE}} q_{\mathrm{NE}}^{\max}$).

To quantify LLI, an additional parameter is necessary. The lithium inventory is the maximum amount of lithium ions available to be lithiated onto or delithiated from electrodes during cycling, including those available beyond the operating voltage window of the full-cell while within the structural limits of both electrodes. A parameter named lithium inventory indicator (LII) can be used to quantify the maximum amount of cyclable lithium ions at the current state, and the change of LII with respect to that at the fresh state is used to estimate the loss of lithium inventory [22,29]. In principle, the LII is expressed as

$$LII = \min(Q_{\mathrm{PE}}^{0}, Q_{\mathrm{NE}}^{100}) - \max(Q_{\mathrm{PE}}^{100}, Q_{\mathrm{NE}}^{0}), \tag{14}$$

where Q_{PE}^{0} and Q_{NE}^{0} represent the capacity values with respect to a stoichiometric index of 0 for the positive and negative electrodes, respectively, and Q_{PE}^{100} and Q_{NE}^{100} represent the capacity value with respect to the stoichiometric index of 1 for the two electrodes. Since the two half-cell potential curves need to be properly scaled and aligned on a common capacity axis to reflect the internal state of a cell, the computation requires knowledge about the remaining active mass on each electrode as well as the stoichiometric offset between the two electrodes. After aligning the half-cell curves on a common capacity axis, Eq. (14) represents the maximum capacity available within the safe stoichiometric limits of the electrodes, with the first term defining the limit at high SOC and the second term at low SOC (both beyond the full-cell operating window). However, in practice, the NE is slightly oversized with an N/P ratio larger than 1, and during a charge cycle, a portion of lithium is retained in the PE to avoid structural damage at very low lithium stoichiometry. As a result, the LII can be simplified by tracking the change of the stoichiometric offset between the two electrodes and the active mass (or capacity) of the PE, which is expressed as

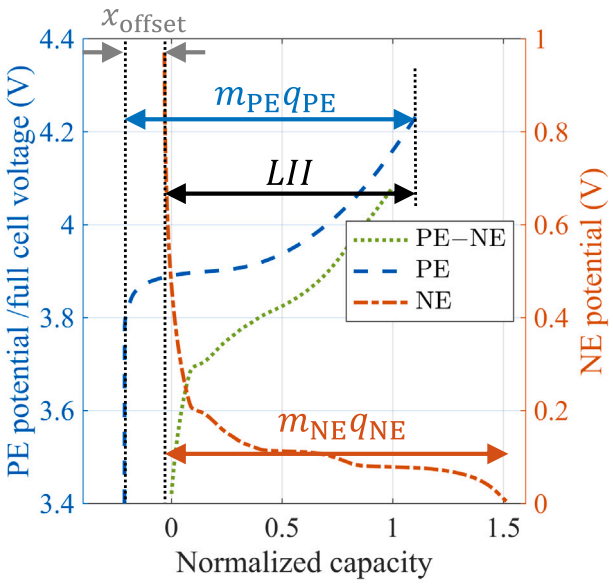

Fig. 5. Overview of degradation parameters $\{m_{\mathrm{PE}}, m_{\mathrm{NE}}, LII\}$.

$$LII = Q_{\mathrm{PE}}^{\max} - x_{\mathrm{offset}}, \tag{15}$$

where the capacity of positive electrode $Q_{\mathrm{PE}}^{\max} = m_{\mathrm{PE}} q_{\mathrm{PE}}^{\max}$ and the capacity offset $x_{\mathrm{offset}} = \delta_{\mathrm{PE}} - \delta_{\mathrm{NE}}$. Note that the offset x_{offset} is defined by the lithium inventory preserved by the stoichiometric offset between the PE and NE, and the equation for x_{offset} calculation is utilized under a fitting reference at the beginning of a full-depth charge. As shown in Fig. 5, LII reflects the maximum amount of capacity to gain between a fully delithiated positive electrode (the right endpoint of the positive electrode half-cell curve) and a fully delithiated negative electrode (the left endpoint of the negative electrode half-cell curve). If a cell is cycled beyond these two endpoints, undesirable structural damage to the electrodes could occur, leading to severe degradation and safety concerns. Also, since these limits are tied to the half-cell curves, the reference remains universal as cells age, allowing consistent quantification of the maximum amount of cyclable lithium ions within the limit. The LLI can be quantified by

$$\mathrm{LLI} = \frac{LII^{\mathrm{fresh}} - LII}{LII^{\mathrm{fresh}}}. \tag{16}$$

3.3. Effects of different aging conditions on the dV/dQ curve

Li-ion batteries can have completely different usage profiles depending on the intended applications. Combinations of various aging stresses, such as cycling rates, ambient temperatures, or SOC ranges during cycling, can impose degradation mechanisms and modes on

cells. A complete analysis of the relationships among the aging stress types, the resulting degradation mechanisms, and the corresponding degradation modes can be found in the seminal work by Birkl et al. [15].

All these degradation mechanisms and the high-level degradation modes leave their corresponding signatures on the pOCV measurements and the associated dV/dQ curves. Changes in the position, intensity, and spacing of peaks in the dV/dQ spectrum reflect shifts in electrode potentials, loss of lithium inventory LLI, and loss of active material LAM. For example, calendar aging dominated by SEI growth primarily consumes cyclable lithium, leading to shifts in electrode stoichiometry balancing and the horizontal movement of dV/dQ peaks [52]. In contrast, degradation involving active material loss produces changes in peak amplitude and broadening due to reduced electrode utilization [53]. Consequently, aging conditions such as temperature, state of charge, depth of discharge, and cycling rate influence the dV/dQ curve indirectly through the dominant degradation pathways they promote [54]. Elevated temperatures and high-SOC storage typically accelerate parasitic side reactions and lithium consumption, whereas aggressive cycling or large depth of discharge can induce structural damage, particle cracking, or loss of active material, all of which manifest as distinct modifications to the differential voltage features [54].

4. Benchmarking studies of degradation diagnostics

This section first provides an overview of the two datasets used in the study. Specifically, we benchmarked different multi-objective fitting scenarios on an experimental emulation dataset with LFP/Gr chemistry and a multi-year aging dataset through various cycling conditions with LCO/Gr chemistry. It then presents individual benchmarking studies for each dataset, followed by a discussion that highlights key findings and suggestions for best practices derived from these studies.

4.1. Dataset description

In this work, to better showcase the quantification of degradation modes using the half-cell model and benchmark different approaches for quantification, we utilize two battery datasets with distinct chemistries and test procedures. The first dataset is an experimental dataset consisting of 11 lab-fabricated LFP/graphite coin cells. This dataset, inspired by the work by Birkl et al. [15], utilizes fresh electrodes for cell fabrication and controls the area and SOC of electrodes to emulate LAM and LLI, respectively. A key objective of the experimental design is to create a dataset that emulates a broad variety of degradation modes, capturing both the severity of each mode and combinations of different modes. A complete list of cells, including the fabrication details and the corresponding expected degradation emulation, is summarized in Table 1, and the detailed experimental procedures are provided in Supplementary Materials Section S1. In brief, all fabricated coin cells are exposed to C/20 constant current cycling up to 8 cycles, and the C-rate of each cell is determined by the theoretical capacity of its LFP electrode. The first three cycles are considered formation cycles, during which some lithium inventory is lost in the formation of the solid-electrolyte interface (SEI). The fifth cycle is used for fitting the half-cell model.

Degradation of lithium-ion batteries results from a complicated combination of electrochemical (e.g., lithium plating, SEI growth, and SEI decomposition) and electromechanical (e.g., particle cracking, loss of electrical contact) processes. Emulating the degradation modes by simply changing material sizes and SOC levels cannot fully reflect the degradation in real application settings, especially when the half-cell data is collected from simple sandwiched coin cells but the full-cell data to be diagnosed is collected from cells of different form factors (e.g., cylindrical, pouch, or prismatic cells), different electrode structures (e.g., jelly rolls, stacked layers, etc.), and most importantly, much larger capacity.

Therefore, we use the second dataset to demonstrate a realistic scenario in which degradation is introduced through a ~4-year aging test campaign, and full-cell data for degradation diagnostics is collected from full-size cells. This dataset consists of 24 implantable-grade LCO/graphite prismatic cells [22,27,29]. These 24 cells are evenly divided into six groups, and each group was exposed to different cycling conditions, with varying discharge rates, ambient temperature, and upper cutoff voltage. The cycling conditions of all groups are summarized in Table 2. These cells are designed for low power usage in implantable devices, and the cycling conditions listed in Table 2 are intended to accelerate degradation beyond typical implantable device usage (by increasing the discharge rate and ambient temperature). For reference, a typical discharge rate for implantable devices is approximately C/168–C/336 (i.e., a full discharge in one to two weeks), and the ambient temperature should be around the temperature of a human being (i.e., 37 °C). Besides the cycling tests under varying conditions, the identical periodic reference performance tests (RPTs) were carried out, in which cells are cycled under the exact same currents, voltage operational windows, and ambient temperature. In this study, we utilize the measurements from the C/50 cycle in RPTs to fit a half-cell model and quantify degradation caused by each mode. In addition to the available RPT data for non-destructive analyses, some cells from this dataset were opened at different stages during the cycling test. Electrode pieces were recovered and paired with lithium metal in coin half-cells to measure the remaining capacity, primarily providing an experimental validation of the remaining active mass on the electrode. The active mass in coin half-cells was obtained by dividing the measured remaining capacity by the mass-specific capacity, which is then scaled up to estimate the remaining active mass on full-size cells based on the area ratio. The information about the disassembled cells, including the total number of RPTs (i. e., the last RPT before disassembly) and normalized remaining capacity before disassembly, is summarized in Table 3. These cells are also assigned condition-based labels for later reference in the benchmarking results and discussions, in the format of (charge rate, discharge rate, ambient temperature).

Raw data collected from battery testers often require preprocessing before entering the modeling workflow, especially at very low cycling rates. The reason is that, even under the same sampling frequency, each cell and each cycle will end up with a different number of data points. To be able to implement the objectives discussed in Section 3.1, it is best practice to interpolate the measured QV curves to the same number of data points, and the interpolation algorithm is usually chosen from the piecewise cubic Hermite interpolating polynomial (PCHIP) and cubic spline. While PCHIP preserves shape and enforces monotonicity (i.e., the capacity measurements of a cell are strictly monotonic), the cubic spline is preferable when measurements are noisy due to its smoothing capability. Both algorithms ensure at least first-order continuity, making the differential curves continuous and easy to manipulate. Also, the number of data points after interpolation should be sufficient to represent the raw QV and dV/dQ curves without losing key phase-change signatures. In this work, the PCHIP interpolator is used to obtain 250 data points from the QV measurements, and the dV/dQ curves are derived from the interpolated QV curves.

4.2. A benchmarking study on the LFP/Gr experimental dataset

To benchmark the capability of using the half-cell model fitting for degradation diagnostics via different predefined fitting objectives, we designed six benchmarking cases, each characterized by a distinct selection of optimization objectives. A summary of these cases is provided in Table 4. In a multi-objective optimization problem, the solution is a set of Pareto-optimal solutions in which no objective can be improved without degrading at least one other objective. To facilitate the interpretation and comparative analysis of results, only one representative solution for each case has been selected. More specifically, the selected

Table 1
Summary of cell fabrication settings and emulated degradation for LFP/Gr experimental dataset.

Cell Name	Electrode Properties				Degradation Emulation		
	PE diameter (mm)	PE SOC (%)	NE diameter (mm)	NE SOC (%)	LAM_{PE} (%)	LAM_{NE} (%)	LLI (%)
Fresh	15	100	16	0	0	0	0
LLI-1	15	90	16	0	0	0	10
LLI-2	15	80	16	0	0	0	20
LAM_{PE}-1	12	0	16	100	36	0	0
LAM_{NE}-1	15	100	12	0	0	44	0
$LAM_{PE,LLI}$-1	12	100	16	0	36	0	36
$LAM_{PE,LLI}$-2	12	90	16	0	36	0	42
$LAM_{NE,LLI}$-1	15	90	12	0	0	44	10
$LAM_{NE,LLI}$-2	15	80	12	0	0	44	20
All mode-1	12	90	12	0	36	44	42
All mode-2	12	80	12	0	36	44	49

Table 2
Summary of cycling conditions for the LCO/Gr aging dataset.

Group	Charge Rate	Discharge Rate	Ambient Temperature	Voltage Window
G1	C/3	C/24	37 °C	3.4 V – 4.075 V
G2	C/3	C/24	55 °C	3.4 V – 4.075 V
G3	C/3	C/3	37 °C	3.4 V – 4.075 V
G4	C/3	C/3	55 °C	3.4 V – 4.075 V
G5	C/3	C/10	37 °C	3.4 V – 4.075 V
G6	C/3	C/24	37 °C	3.4 V – 4.175 V

Table 3
Summary of full-cell disassembly for the LCO/Gr aging dataset.

Cell	Condition-based Label	Remaining Capacity (%)
G1C1	(C/3, C/24, 37 °C)	95.3
G2C3	(C/3, C/24, 55 °C)	87.9
G3C1	(C/3, C/3, 37 °C)	89.3
G4C3	(C/3, C/3, 55 °C)	79.1
G1C3	(C/3, C/24, 37 °C)	88.6
G2C1	(C/3, C/24, 55 °C)	73.6
G3C3	(C/3, C/3, 37 °C)	85.8
G6C1	(C/3, C/24, 37 °C)	90.8

Table 4
Benchmarking cases by number of selected optimization objectives.

Case Number	Number of Objectives	Selected Objectives to Optimize
1	1	MSE_{QV}
2	2	MSE_{end}, MSE_{QV}
3		MSE_{peaks}, $MSE_{dV/dQ}$
4	3	MSE_{end}, MSE_{QV}, MSE_{peaks}
5		MSE_{end}, MSE_{QV}, $MSE_{dV/dQ}$
6	4	MSE_{end}, MSE_{QV}, MSE_{peaks}, $MSE_{dV/dQ}$

solutions are those with the smallest normalized distance to the Utopia point, which is a hypothetical, unattainable point representing the lowest value of each objective within the set of Pareto-optimal solutions. In general, this "balanced" solution is a well-rounded trade-off among all optimization objectives, providing a good representation of the overall degradation behavior inferred from the measurements (i.e., QV and dV/dQ curves). There are two major evaluation criteria considered in this benchmarking study: (1) the overall fitting performance between the measured and reconstructed curves, quantified by objective function values, and (2) the discrepancy between the estimated health parameters from half-cell model fitting and the expected parameters based on cell fabrication. Four representative cells exhibiting distinct degradation behaviors are presented in Fig. 6 to illustrate degradation parameter alignment and to compare overall fitting performance across the six benchmarking cases. Results from all cells in the LFP/Gr dataset are provided in the Appendix: Fig. A.2 shows the evolution of the four objective values with respect to the optimization setups, Fig. A.3 shows the comparison between experimental and reconstructed curves, and Fig. A.4 shows the estimated degradation parameters corresponding to each case. In general, since this dataset emulates all different degradation modes with pristine materials and has no significant difference in form factor or other characteristics between half-cells and full-cells, the improvements on half-cell model fitting performance from utilizing multi-objective optimization may be marginal in some cells, but it still provides valuable insights into choosing different fitting strategies in realistic applications.

The first case serves as the baseline, utilizing a single objective to optimize the overall fitness of QV curves (MSE_{QV}), which has been applied in previous literature [15,30]. As expected, this optimization configuration results in the lowest normalized value of MSE_{QV} across all other cases (for the same cell), as shown in Fig. 6(i–l). The second and third benchmarking cases provide more comprehensive fitting strategies, with two optimization objectives targeted to either the QV curve (MSE_{end} +MSE_{QV}) or the dQ/dV curve (MSE_{peaks} +$MSE_{dV/dQ}$). When both MSE_{end} and MSE_{QV} are jointly optimized, we observe a better alignment of the QV end points, as confirmed by the significant decrease in the values of MSE_{end} while MSE_{QV} values remain fairly consistent with their respective Case 1 values (see Fig. 6(i–l)). Also, since the reconstructed QV curves from the half-cell model are bounded by the total capacity, the lower MSE_{end} error stands for lower discrepancy between the start and end terminal voltage, indicating more accurate fitting to the total charged capacity by the half-cell model. On the other hand, if only MSE_{peaks} and $MSE_{dV/dQ}$ are optimized, the key characteristics on the QV curve are completely neglected, resulting in significant increases in MSE_{end} and MSE_{QV} values. Objectives targeting the QV curve provide well-rounded fits, whereas objectives targeting the dV/dQ features can aid in parameter estimation accuracy under specific degradation modes. This is further demonstrated in Fig. 7, where optimizing MSE_{end} +MSE_{QV} +MSE_{peaks} objectives results in improved alignments of dV/dQ peaks across all emulated degradation modes.

Notably, the normalized value of $MSE_{dV/dQ}$ does not change significantly between cases where $MSE_{dV/dQ}$ is included in the optimization (Cases 3, 5, 6) versus when it is not (Cases 1, 2, 4), except for cells with the LAM_{PE}-1 degradation mode. In this degradation state, including the $MSE_{dV/dQ}$ objective during optimization reduces parameter estimation error for m_{PE}, as shown in Fig. 6(g), but at the same time increases the error in estimating LII. By looking at Fig. 6(c), the estimated m_{PE} and LII are nearly equal in each optimization case. Similarly, for the other two cells highlighted in Fig. 6(b, d), the half-cell model cannot differentiate the degradation mode LAM_{PE} and LLI. The dominant reason is that LFP electrodes exhibit a two-phase reaction during charge and discharge, which is reflected in the capacity-potential curve as a potential plateau. The potential plateau makes half-cell model fitting challenging, as it hinders matching curve characteristics to the experimental full-cell QV curves. Intuitively, since the potential plateau exists, either expanding/shrinking by adjusting m_{PE} or shifting by adjusting

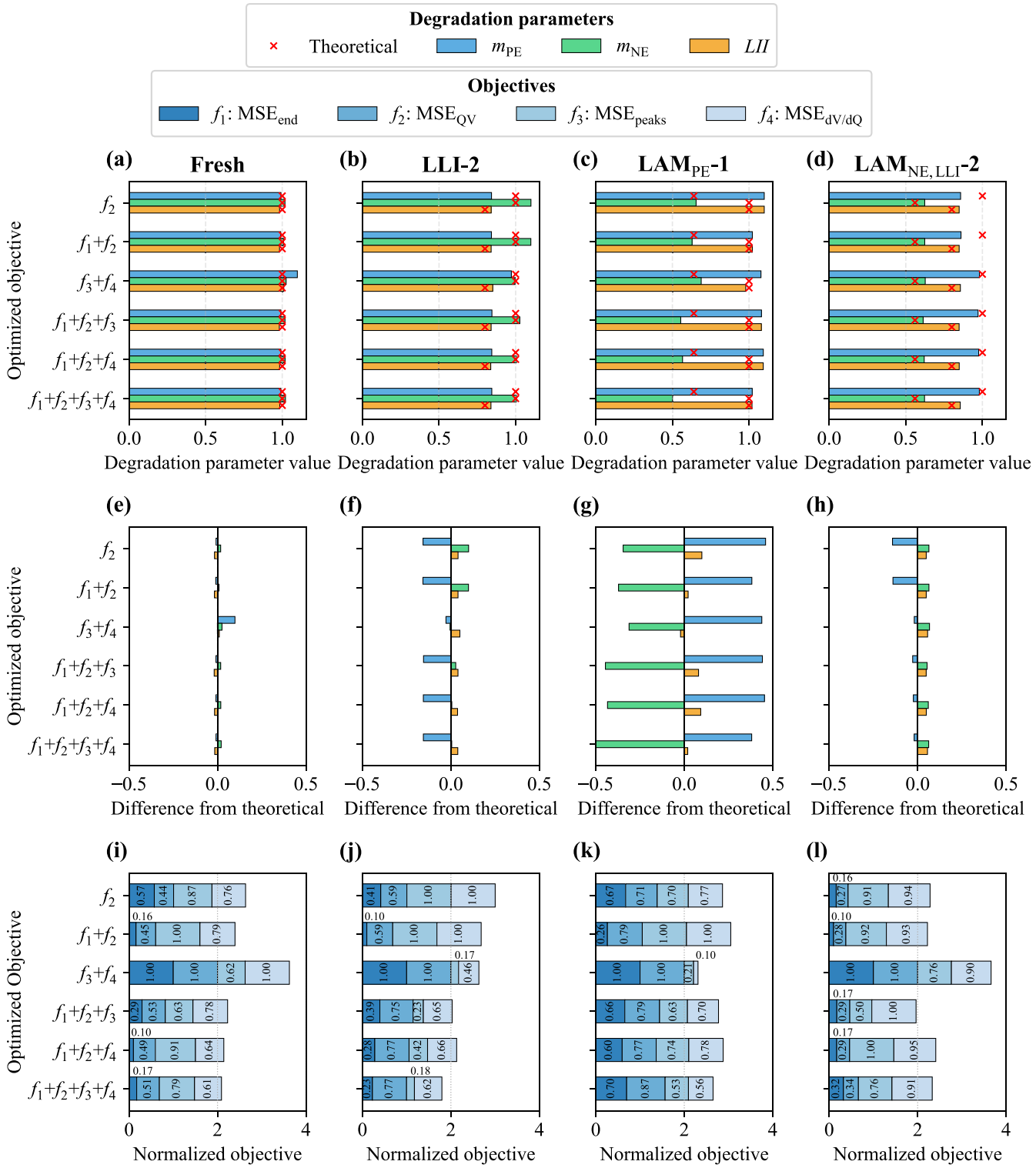

Fig. 6. Comparison of benchmarking results for four selected cells from the LFP/Gr experimental emulation dataset and all six benchmarking cases: (a–d) estimated degradation parameters against the expected emulation; (e–h) difference between the estimated and emulated degradation parameters; (i–l) normalized objective values (each objective is normalized to the interval [0.1, 1.0] to enhance readability).

δ_{PE} would cause similar effects on the change in the full-cell simulated curve after superposition with the graphite half-cell curve. For the same cell LAM_{PE}-1, the estimated m_{NE} is significantly lower than the theoretical values, which is consistent throughout all optimization setups. The high discrepancy of m_{NE} is neither due to numeric errors nor issues with the optimization, but the result of a high N/P ratio (the ratio between negative and positive electrodes). The theoretical value is calculated based on the nominal mass of the electrode to its size, assuming full exposure to relatively uniform lithiation and delithiation. However, in cells with a high N/P ratio, the overhanging portion of the much larger

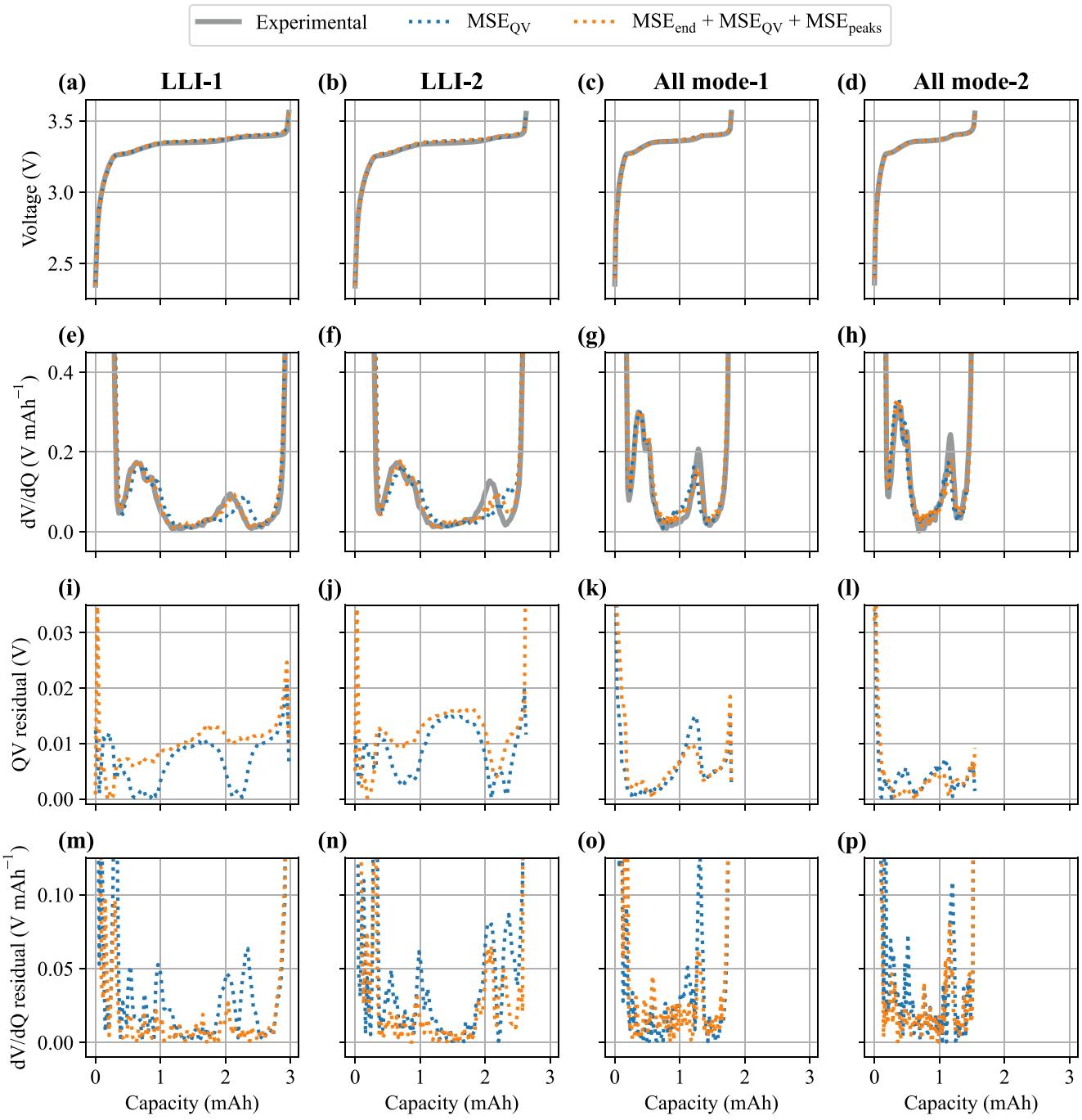

Fig. 7. Comparison between the simulated QV and dV/dQ curves for four selected cells from the LFP/Gr experimental emulation dataset and two selected benchmarking cases. (a–d) The fitted QV curves obtained using single-objective (MSE_{QV}) and multi-objective (MSE_{end} +MSE_{QV} +MSE_{peaks}) optimization compared against the experimental QV curves; (e–h) comparisons for the corresponding differential capacity (dV/dQ) curves; (i–l) residuals between experimental and simulated QV curves; (m–p) residuals between experimental and simulated dV/dQ curves.

graphite electrode is not fully utilized for lithiation/delithiation. Thus, the actual "active" mass on the graphite electrode is much less than the nominal value. More discussions on behaviors specifically to cells with a high N/P ratio are included in Section 4.2.1.

4.2.1. Discussion on half-cell model fitting performance on coin cells with high n/p ratio

The emulation of active material loss via disproportionate electrode areas is limited by non-uniform lithiation during cycling. Specifically to this study, the larger N/P ratio leads to non-uniform lithiation of the graphite anode, with the anode area overlapping with the LFP reaching a higher degree of lithiation than the non-overlapping area. This is because the electrical field in the non-overlapping area is weaker, and the ion-transport path is longer between these areas and the LFP cathode. The non-uniform lithiation of graphite in high N/P ratio cells has been well-documented in both experimental and computational studies in literature [55,56] and our own study. This issue affects both the SEI formation and the actual utilization of the larger electrode, which deteriorates the quality of half-cell model fitting and the degradation mode quantification.

Based on the half-cell model fitting results shown in Fig. 8(a–b), a sharp peak is observed in the experimental dV/dQ curve in cells with

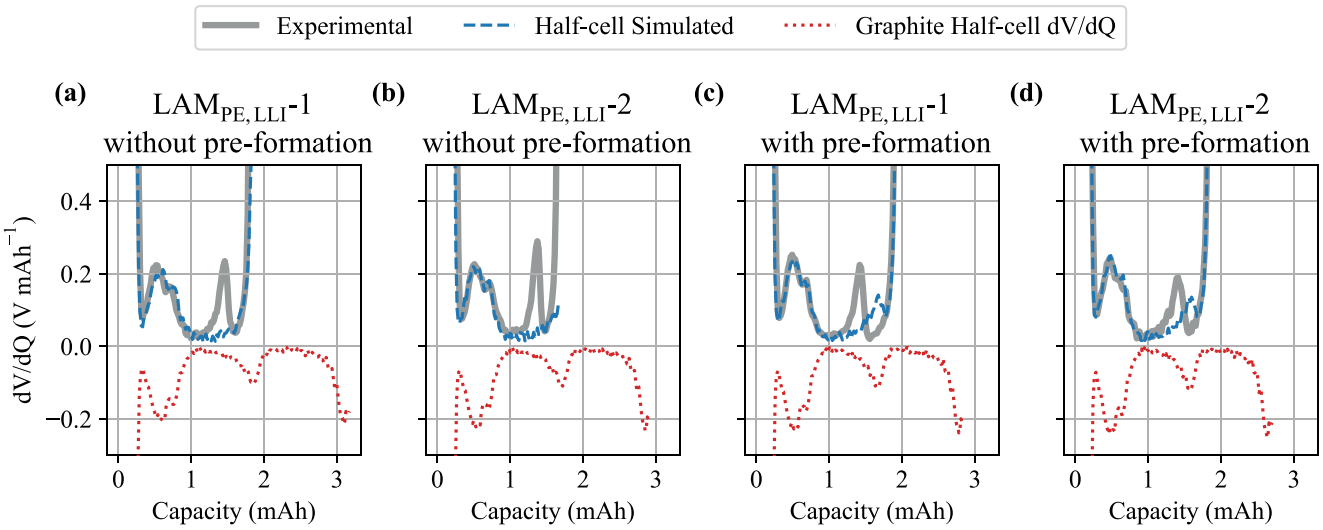

Fig. 8. Comparison of half-cell simulated and experimental dV/dQ curves for cells with high N/P ratios. (a–b) Two cell configurations without graphite pre-formation; (c–d) the same configurations, but with graphite pre-formation.

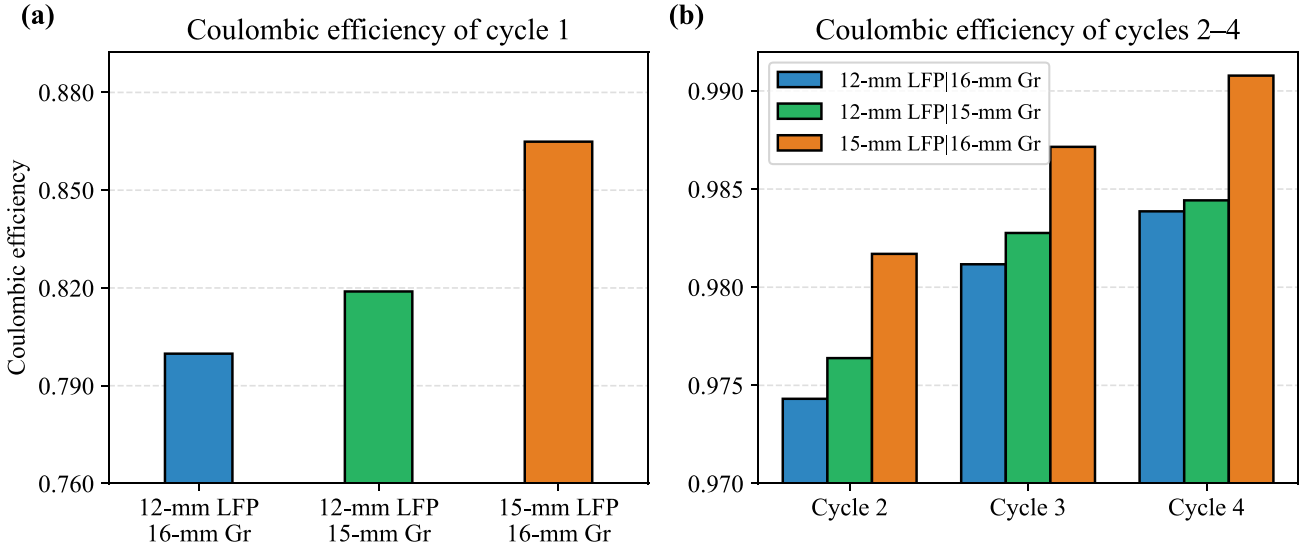

Fig. 9. Coulombic efficiency of cells with different N/P ratios at (a) cycle 1 and (b) cycles 2–4.

16-mm fresh graphite as anodes and 12-mm fresh LFP (for LAM$_{PE,LLI}$-1) or 12-mm 10% discharged LFP (for LAM$_{PE,LLI}$-2) as cathodes, respectively. Different from the other types of cells, this peak is not well aligned with the data fitted by the half-cell models. It is known that the peaks in dV/dQ curves of graphite half-cell represent the three stages of graphite phase transition as lithiation of graphite progresses, i. e.

$$C_6 \xrightarrow{\text{Stage 3}} LiC_{24} \xrightarrow{\text{Stage 2}} LiC_{12} \xrightarrow{\text{Stage 1}} LiC_6.$$

The non-uniform lithiation of graphite can cause the same phase transition to occur in different electrode regions at varying potentials, resulting in peak shifts, splits, or merges. This makes it extremely challenging to fit the graphite half-cell curve, which was measured from a half-cell with uniform lithiation, to the data of full cells with a high N/P ratio shown in Fig. 8(a–b). The heterogeneous lithiation of graphite also suggests a heterogeneous growth of SEI, as both processes are influenced by the same factor (i.e., the local electric field and Li^+ ion transport from LFP). Furthermore, heterogeneous SEI coverage on graphite exacerbates heterogeneous lithiation by altering local electronic and ionic conductivities. Such heterogeneous lithiation is evidenced by the different coloration on graphite between the region overlapped with the 12-mm LFP and the overhanging region, as observed from disassembling a cell with a 12-mm LFP and 16-mm graphite after formation (see Figure S2 in the Supplementary Materials). To homogenize lithiation in full cells with high N/P ratios, we constructed such cells with graphite anodes pre-formed with 16-mm LFP cathodes at C/20 for two cycles. This pre-formation is expected to produce more homogeneous SEI coverage on the graphite and, consequently, more homogeneous graphite lithiation. These pre-formed graphite anodes were then disassembled and reassembled into full cells with 12-mm LFP electrodes at 100% or 90% SOCs to produce full cells with a high N/P ratio. As illustrated in Fig. 8(c–d), full cells composed of 12-mm LFP and 16-mm graphite with pre-formed graphite anodes exhibit a closer match to the curves reconstructed by the half-cell model compared with identically sized cells utilizing fresh graphite anodes.

The heterogeneous growth of SEI with high N/P ratio cells is also supported by comparing the Coulombic efficiency (CE) of formation cycles among cells with different N/P ratios. Two cells with lower N/P ratios were included, one with a 12-mm LFP and a 15-mm graphite, and the other one with a 15-mm LFP and a 16-mm graphite (i.e., the cell "Fresh" in this dataset), respectively. From Fig. 9(a), the 15-mm LFP|16-mm Gr cell demonstrates the highest CE of the first cycle at

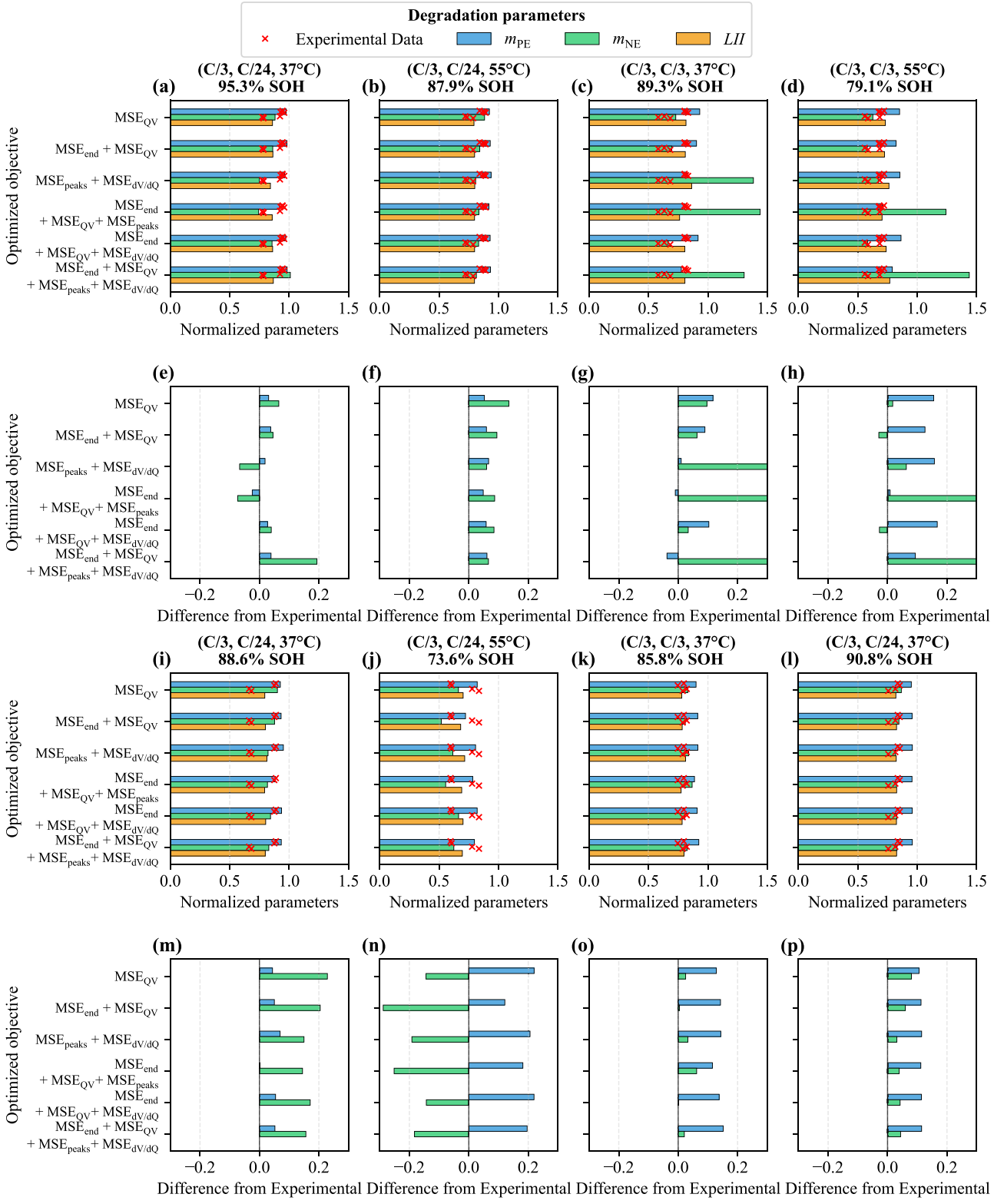

Fig. 10. Comparison of estimated degradation parameters against the experimental validation for all six benchmarking cases on LCO/Gr cycling aging dataset. (a–d) and (i–l) Comparison between estimated and experimentally validated degradation parameters for cells; (e–h) and (m–p) differences between the estimated and the mean of the corresponding experimental data.

86.5% compared to the other two types of cells with a higher N/P ratio. Moreover, the first-cycle CE exhibits a descending trend as the N/P ratio increases, indicating that more active lithium ions are consumed during the formation of the SEI, resulting in greater irreversible capacity loss and a lower SOC level of the LFP after the first cycle. Compared to the first cycle, the CE increases to around 98% for all three cells in the second cycle and stabilizes while slightly increasing onwards (Fig. 9(b)). This indicates that the majority of SEI formation was completed during the first two cycles. Consistent with the first cycle, cells with lower N/P ratios show higher CE in each subsequent cycle, from cycle

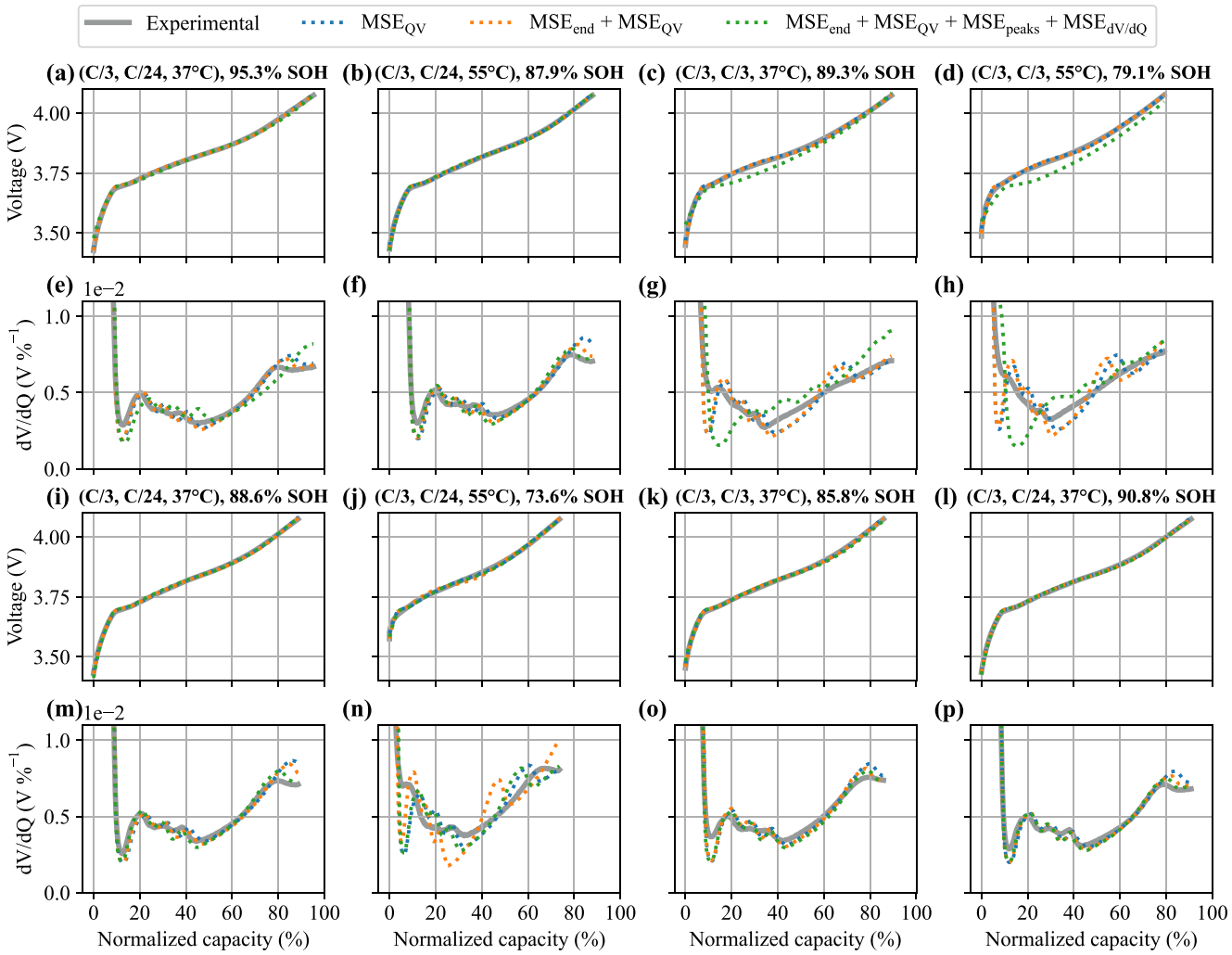

Fig. 11. Comparison between the simulated QV and dV/dQ curves for three selected benchmarking cases (MSE$_{QV}$ only, MSE$_{end}$ +MSE$_{QV}$, and MSE$_{end}$ +MSE$_{QV}$ +MSE$_{peaks}$ +MSE$_{dV/dQ}$) on LCO/Gr cycling aging dataset.

2 to cycle 4. These results reveal that irreversible capacity loss is more significant in cells with higher N/P ratios, likely due to the continuous growth of SEI.

This study provides two important highlights for experiments involving cells with a high N/P ratio. First, if cells with a high N/P ratio are desired for any study, pre-formation of graphite or other anode materials on cells with a low N/P ratio is required to form a high-quality SEI layer. The high-quality SEI layer delivers more homogeneous phase changes during cycling, allowing better evaluation of cell performance. Second, even with the pre-formation to homogenize SEI growth during formation cycles, utilizing cells with a high N/P ratio to emulate only a high-level LAM$_{PE}$ is not a valid approach. In such cell configurations, the anode is not fully utilized due to the non-uniform lithiation in the overhanging region, resulting in an undetermined emulation of LAM$_{NE}$.

4.3. A benchmarking study on the LCO/Gr aging dataset

Similar to the study on the LFP/Gr experimental dataset, the same six benchmarking cases described in Table 4 are demonstrated on this multi-year aging dataset. As mentioned in Section 4.1, eight cells were disassembled for aged half-cell construction, validating the estimation of m_{PE} and m_{NE}. In this benchmarking study, data from the last RPTs of these eight cells (see Table 3 for details) are used, and the estimated degradation parameter values are compared with experimental measurements. Fig. 10 visualizes the estimated degradation parameters for all eight cells based on different optimization setups, overlaying with all data points from the experimental validation. The reconstructed QV and dV/dQ curves from the half-cell model in three representative optimization cases (i.e., MSE$_{QV}$ only, two QV objectives, and all four objectives) are visualized against the measured data in Fig. 11 (refer to Fig. A.5 for the results of all six benchmarking cases).

From Fig. 10, we observe improvements in estimating the degradation parameters, compared to the experimental validation results, by incorporating multiple objectives for half-cell model fitting, with the exceptions of (C/3, C/3, 37 °C) at 89.3% SOH and (C/3, C/3, 55 °C) at 79.1% SOH. As shown in Fig. 10(g,h), the accuracy of degradation parameter estimation deteriorates when incorporating objectives from dV/dQ curves. Issues caused by adding dV/dQ-based objectives can be largely attributed to the significant distortion of dV/dQ curves from these three cells. Distorted dV/dQ curves impact the meaningfulness of including both the MSE$_{dV/dQ}$ and MSE$_{peaks}$ objectives. As shown in Fig. A.6(c,d,f), the number of identified peaks from distorted curves varies, which will fail to align the same peak on half-cell reconstructed dV/dQ curves. In these cases, dV/dQ objectives provide misleading information to the optimization. However, simply by adding the MSE$_{end}$ objective for matching QV endpoints, the phase change alignments (i.e., peak locations and shapes) show improvements for all cases where peaks on dV/dQ curves are identifiable. For other cases, we do observe the benefits of multi-objective optimization incorporating signatures on dV/dQ curves, especially in further aligning phase-change physics.

For example, in Fig. 11(e,m,o,p), although there are no noticeable differences in QV curve fitness across three representative cases, the peaks in dV/dQ curves align much better by comparing the blue dotted curves (MSE_{QV} only) and the green dotted curves (all four objectives). Such improvements in overall fitting also reflect on the change in objective values, which can be interpreted as goodness-of-fit metrics, across different cases (as shown in Fig. A.7). Notably, there are increases in the overall goodness of fit, as evidenced by lower sums of overall normalized objective values, highlighting the positive contributions of multiple objectives. One exception is when the fitting process solely relies on the two dV/dQ objectives, which is the worst among all multi-objective optimization cases, sometimes even worse than the respective single-objective cases. This observation again highlights the impracticability of relying solely on dV/dQ objectives to guide the half-cell model fitting process.

Three additional studies are conducted on this dataset to further assess the applicability of multi-objective setups in realistic use cases. First, we perform a comparative study on capturing the degradation trajectory, demonstrated on six cells — one cell per group — across their entire time-on-test. The degradation trajectories are then compared with the manual fitting results from the work by Navidi et al. [29], which are both visualized in Fig. A.8. The procedure for manually fitting the half-cell model to pOCV is summarized in Appendix A.2. More specifically, we use the two QV objectives and NSGA-II to perform automatic fitting. The multi-objective optimization results tend to fluctuate throughout the test, mainly on the estimation of m_{PE} and m_{NE}. This is due to the unconstrained optimization setup during the automatic fitting process. To enforce monotonicity, the history of degradation parameters must be known to adjust the upper bound of m_{PE} and m_{NE} in each iteration. This will limit the application of such a degradation diagnostics technique on cells with an unknown history. For the manual fitting results presented in [29], the monotonic trend in degradation parameters is enforced by sequentially fitting each RPT of a cell. Also, there is a large discrepancy between automatic and manual fitting results, especially for substantially aged cells, and the discrepancy can reach up to 20%. Since, by no means, manually aligning overall fit or matching endpoints is more accurate than mathematically minimizing the MSE of these between measured and half-cell simulated curves, the alignment of captureable signatures on QV curves should always be better via optimization. However, since there is no ground truth about the degradation path throughout the test time available, it remains an unsolved problem worth further investigation. A brief discussion about the advantages and disadvantages of manual fitting compared to automatic fitting is also included in Appendix A.2.

The second study is a parametric study in which we scalarize the two QV objectives by assigning different weights to them. The scalarized objective is defined as $f_s = \alpha \times \mathrm{MSE}_{end} + (1-\alpha) \times \mathrm{MSE}_{QV}$, and the weight α is sampled from the discrete set $\{0.1, 0.2, \ldots, 0.9\}$. The details of implementation are explained in Section S3 of the Supplementary Materials. In brief, when a weight of α between 0.3 and 0.5 is assigned to the MSE_{end} objective, the overall fitting measured by MSE_{QV} remains consistent, but the fitting of the endpoints improves. Additionally, based on our previous analyses of benchmarking performance, a better fit to the endpoints results in improved alignment of the phase-change peaks on dV/dQ curves. This study suggests that the multi-objective optimization problems presented in this work can be simplified into a single-objective optimization problem (only to optimize f_s), making it easier for practitioners to implement.

The third study evaluates the proposed method under conditions where full-cell measurements are available only over a limited SOC window. Two cells are considered: one exhibiting dV/dQ distortion and the other without such distortion. Model fitting is performed using data restricted to the 50%–100% SOC range. To accommodate this constraint, a minor modification is introduced by adding a parameter to estimate the charged capacity at the start of the partial segment, while preserving the original four-parameter half-cell model structure. Detailed methodology and corresponding results are provided in Section S4 of the Supplementary Materials.

When the optimization is limited to partial-SOC data, model identifiability is inherently reduced, particularly when key informative features (e.g., curvature and peak structures) are predominantly concentrated in the low-SOC region. Although the proposed method achieves good agreement within the fitted SOC window, substantial discrepancies arise between the reconstructed and measured curves outside this range. These deviations are primarily attributed to inaccuracies in parameter estimation, which subsequently propagate to errors in degradation mode quantification.

Improving performance under such constraints may require more sophisticated half-cell models or tailored optimization strategies. However, these approaches are beyond the scope of this work and warrant further investigation. More broadly, these results highlight an important research direction of developing robust methods that account for degradation-induced changes in measurements to enable accurate model parameterization from limited data. This challenge extends beyond half-cell models and is relevant to other physics-based and empirical modeling frameworks.

4.4. Uncertainty quantification for estimated degradation parameters

When using the multi-objective optimization framework to fit the half-cell model, the solution space consists of Pareto-optimal solutions. In many practical applications, only point estimations for the degradation parameters are necessary to evaluate the cell. However, since half-cell model fitting is an inverse parameter identification problem, the quality of uncertainty quantification is valuable for evaluating identifiability. To help understand parameter identifiability in the half-cell model, we conducted a study to quantify uncertainty using approximate Bayesian computation (ABC). ABC has been widely used to estimate posterior distributions when no analytical likelihood can be derived. This property makes it suitable for the half-cell model fitting problem in this work.

In this study, an ABC algorithm with sequential Monte Carlo sampling is implemented through the PyABC package [57]. ABC starts with proper prior distributions for each half-cell model parameter. To align with the assumption in multi-objective optimization settings where the parameters are bounded, the priors are uniform distributions spanning the respective parameter intervals. Then, the sequential Monte Carlo sampler samples model parameters from the prior, which are then used to generate simulated data from the half-cell model. Using the simulated data, a distance metric between the simulated and observed data is calculated, which, in this case, is an equal-weighted sum of MSE_{end} and MSE_{QV}. A limitation of ABC is that it only supports a single scalar distance metric. Samples with the distances below a tolerance threshold are retained as an approximate posterior distribution of the half-cell model parameters. More details about ABC and different sampling strategies can be found in a related tutorial article [58].

Two cells from the LCO/Gr cycling aging dataset, one from mid-life and one from late life, are selected to compare posteriors and the distribution of Pareto-optimal solutions from the NSGA-II case of MSE_{end}+ MSE_{QV}. The results are visualized in Fig. 12 with the histograms normalized to probability density. In general, the Pareto-optimal solutions from NSGA-II show substantial overlap with the ABC posterior distributions for all degradation parameters, indicating that deterministic optimization identifies parameter sets consistent with the uncertainty-aware inference. While the posterior distributions exhibit broader spreads due to the limited identifiability in this inverse problem, the Pareto-optimal solutions cluster near the posterior modes. Such overlap between the Pareto set and the ABC posterior further suggests that the dispersion of Pareto solutions captures a meaningful portion of the uncertainty structure inferred from the data, which can be interpreted as a qualitative measure of parameter identifiability.

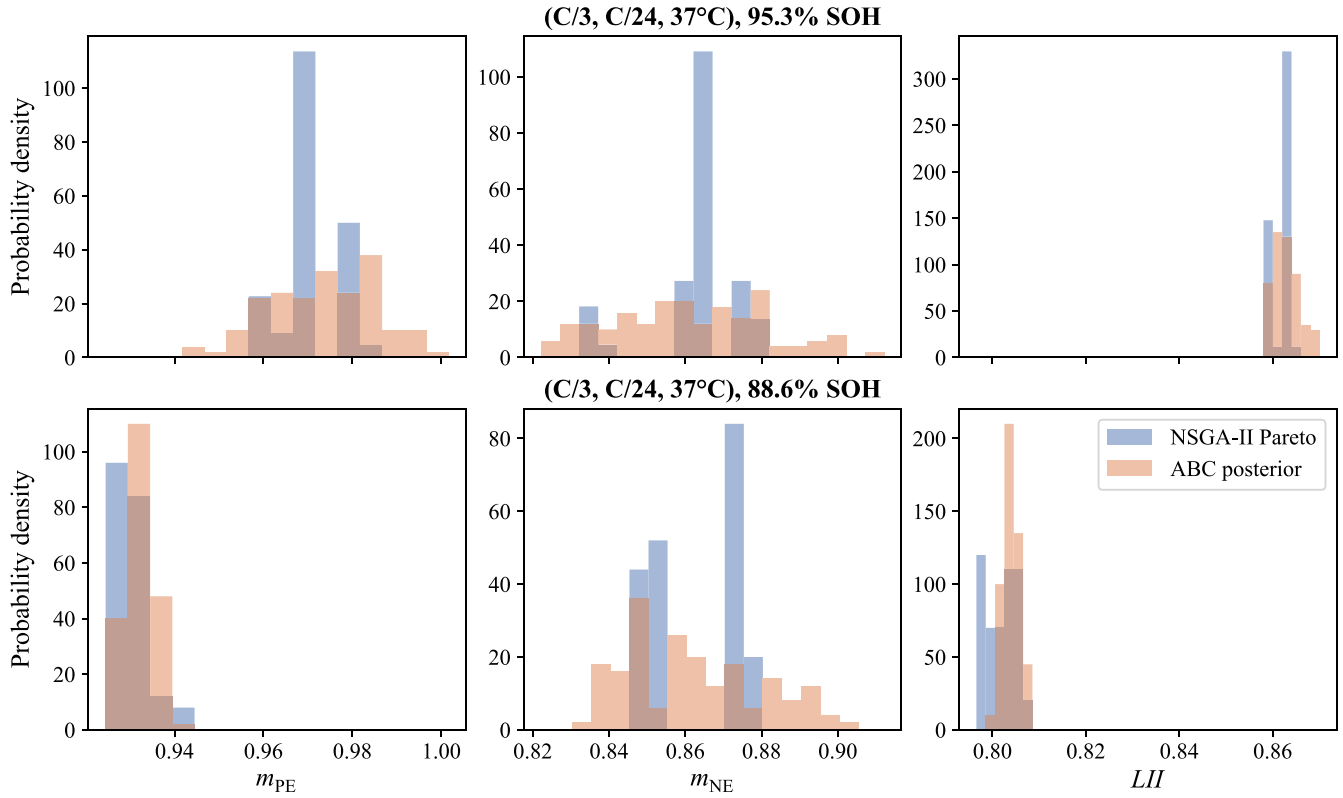

Fig. 12. Comparison of degradation parameter distributions inferred by NSGA-II and ABC for two cells from the LCO/Gr cycling aging dataset.

Besides the uncertainty arising from parameter identifiability, there is also uncertainty associated with measurements (e.g., measurement noise, equipment accuracy, environmental fluctuations). In this study, however, this source of uncertainty is expected to be relatively small because the data were collected under controlled laboratory conditions using calibrated instrumentation and standardized testing protocols. As a result, the variability observed in the inferred parameters is dominated by model non-uniqueness rather than measurement error. For field data and large-scale deployment, where operating conditions are less controlled and sensing accuracy may vary, measurement-related uncertainties are likely to play a more significant role. These practical considerations, along with strategies for robust inference under real-world conditions, are discussed in Section 4.6.

4.5. Key findings and best practices for half-cell model fitting

With the two benchmarking studies on datasets with different cell chemistries and degradation paths (one emulated and one aged through cycling), we fully examine the proposed multi-objective optimization framework for degradation diagnostics using the half-cell model. In general, the multi-objective optimization framework improves the overall fitting compared to a single-objective setup, only optimizing MSE_{QV}. Key takeaways from these two studies are summarized as follows, which can also serve as the best practices for practitioners or researchers aiming to utilize this non-intrusive technique to identify the degradation states of cells at the component level. Note that these conclusions may only hold under the proper data processing steps recommended in Section 4.1 (i.e., **interpolation of the same number of data points per QV curve using PCHIP or, in the case of a higher signal-to-noise ratio, cubic spline for additional smoothing**).

First and foremost, robust half-cell model fitting should **focus on QV objectives**, and **dV/dQ objectives complement the fitting** by providing information related to the electrochemical processes at different SOC levels, especially the MSE_{peaks} objective. As visualized in Fig. A.5(c–d,h–j), only optimizing MSE_{peaks} and $MSE_{dV/dQ}$ can deviate the fitted QV curves from the experimental measurements significantly. This highlights the challenge of generating good fits from using dV/dQ objectives as standalone objectives. However, even when the two dV/dQ objectives are just included to complement QV objectives for optimization, attention to the shape of the dV/dQ curves is required. If the degraded cells exhibit significant distortion on the dV/dQ curves compared to the pristine stage, enforcing MSE_{peaks} and $MSE_{dV/dQ}$ objectives will impose negative effects on the fitting results (as discussed in Section 4.3 and shown in Fig. 11(c,d,j)). Additionally, to accurately locate peaks on dV/dQ curves, **adjustments to parameters of peak identification functions** in various computational packages are necessary. These adjustments require prior knowledge of cell chemistry and the expected evolutionary trends in the dV/dQ curve resulting from degradation. In this work, we used the "find_peaks" function in the SciPy package [59], and we adjusted the parameters "distance" and "prominence" for different datasets. Specifically, the distance parameter needs to account for the resolution (i.e., the number of data points after interpolation) and the expected SOC windows between major peaks, while the prominence requires the consideration of the absolute magnitude of dV/dQ values, making sure the prominence is set at a proper level that filters out jittering measurements but keeps the desired peaks from phase transition. Even when these parameters were carefully adjusted, some small peaks can still be missed. For example, as shown in Fig. A.6(a), although the cell (C/3, C/24, 37 °C) at 95.3% SOH does not have significant distortions on the shape, one of the small peaks cannot be identified properly, leading to the missing of one peak and potential failure in correctly matching peaks with the half-cell simulated curve. So, if the merging or disappearance of peaks is expected at an aged state, such as cells in Fig. 11(g,h,n), one workaround will be to **focus only on one or two major peaks** that are always, or at least most of the time, identifiable. Also, to avoid breaking the optimization due to mismatched peaks, conditional statements to check the peak number on both simulated and measured dV/dQ curves can be introduced before calculating the MSE_{peaks} objective. A simplified flowchart in Fig. 13 provides a high-level summary of the recommendations for objective selections case-by-case.

Second, the performance of the half-cell model fitting is heavily influenced by the **phase change behavior of electrodes** and by the

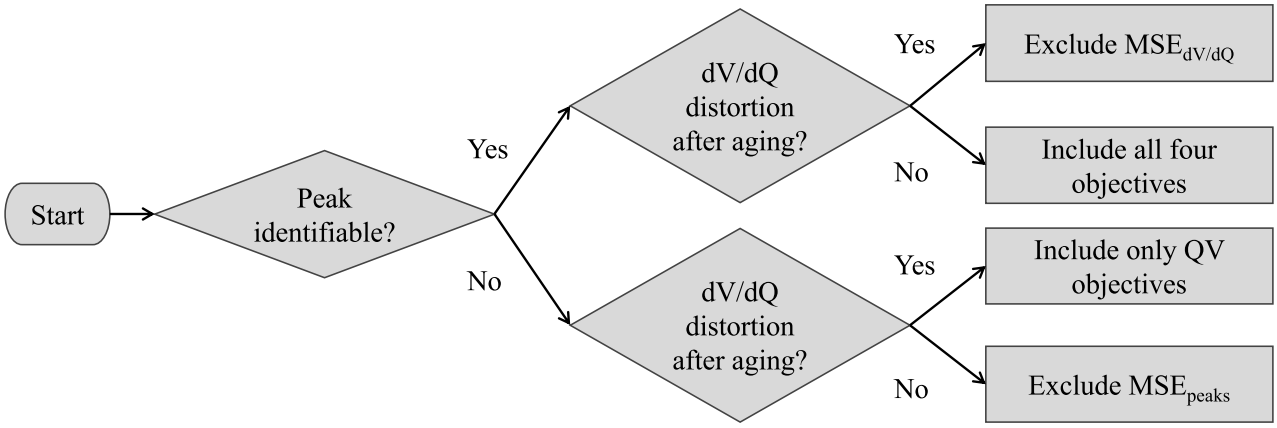

Fig. 13. A flowchart summarizes the general recommendations for objective selections based on the properties observed or assumed based on the specific dataset.

curvature of capacity-potential curves. For LCO, NMC, or NCA cathodes and graphite anodes, the electrode potential changes with SOC, allowing better capture of stoichiometric effects across different aging states and active mass changes. On the other hand, electrodes with a plateau on their potential-voltage curves, such as the LFP cathode or lithium titanate (LTO) anode, can pose difficulties in differentiating degradation modes LAM (either LAM_{PE} for cathode or LAM_{NE} for anode) and LLI. This effect can be found in Fig. 6(b–d) and additional cells in Fig. A.4(b,h).

Third, although the multi-objective optimization algorithms (NSGA-II and NSGA-III) and the multi-objective framework for half-cell model fitting have been demonstrated to be effective for degradation diagnostics, some customization is required for new datasets or implementation cases on the proposed approach. More specifically, the **lower and upper bounds need to be adjusted** for the four half-cell model parameters (m_{PE}, m_{NE}, δ_{PE}, and δ_{NE}) accordingly. Without proper bounds on these parameters, the half-cell model may encounter errors during optimization. Given that the evolutionary optimizer for finding global minima has freedom to span across the entire parameter space bounded by those preset bounds, errors will occur when the active mass values are too small, and the slippage parameter values are too large, resulting in no overlapping region on the superposition of QV and dV/dQ curves between positive and negative electrodes. **Additional parameters for NSGA-II and NSGA-III need to be tuned** based on the complexity of curve fitting, including the population size, the number of generations, and the number of reference directions specific to NSGA-III. For both datasets, a population size of 50 and 100 generations is utilized for all three optimization algorithms (ordinary genetic algorithm, NSGA-II, NSGA-III), and the number of reference directions for NSGA-III is set to 8. These numbers allow proper convergence on both datasets, and they are suggested if the half-cell model fitting problem is not significantly more difficult than the problems presented in this work. A sensitivity analysis is conducted in Section S5 of the Supplementary Materials, where different hyperparameter configurations are evaluated by varying the population size, crossover probability, and mutation probability. The results showed that the optimizer converges successfully within 60 iterations with a population of only 30 samples. A population size of 50 or 100 samples significantly accelerates convergence and reduces run-to-run variation, despite the randomness introduced by sample initialization. Thus, it highlights the robustness of the proposed multi-objective optimization framework against sub-optimal hyperparameter tuning.

4.6. Practical application considerations

Next-gen electrodes and form factors. While the present study benchmarks LFP/Gr and LCO/Gr cells, the proposed multi-objective fitting framework is not inherently limited to these chemistries, as it enforces consistency between the measured full-cell pOCV and dV/dQ response and the reconstructed pOCV from half-cell potentials. As discussed earlier, fitting performance is strongly influenced by electrode phase transition behavior and the curvature of the electrode potential curves [60]. Nevertheless, extending the framework to next-generation systems introduces important considerations.

For nickel-rich NMC or NCA cells, the number, position, and intensity of phase transition peaks in dV/dQ may evolve with aging and increasing polarization, which can affect the MSE_{peaks} objective when peak identification is applied without chemistry-specific constraints. In such cases, restricting the objective to the most persistent transitions or using feature windows instead of strict peak-to-peak matching can preserve identifiability [32]. For silicon-blended graphite anodes, degradation can modify not only the horizontal position but also the effective shape of the anode potential curve due to loss of active silicon and increasing hysteresis [61]. This behavior partially violates the pure shift-and-scale assumption used in half-cell reconstruction. A practical extension is to introduce limited, regularized shape flexibility or to employ a library of aging-dependent anode curves, while retaining the same multi-objective structure. For solid-state cells, larger interfacial impedance and slower relaxation may cause the measured low-rate QV curve to deviate from true equilibrium behavior, as solid–solid interfaces can develop space-charge layers and highly resistive interphases that lead to sluggish charge-transfer kinetics [62]. In this case, stricter near-equilibrium acquisition, explicit ohmic/polarization correction, or inclusion of a small SOC-dependent bias voltage term may be required to ensure that the fitting parameters remain physically interpretable.

Overall, the multi-objective formulation remains applicable across material systems because it does not rely on a specific voltage shape. However, its practical implementation should be tailored to the phase-transition characteristics, peak observability, and stability of the reference half-cell potentials for the chemistry under consideration.

Runtime and practical deployment considerations. The cost of the optimization is dominated by repeated evaluations of the QV curve reconstruction and fitting, during which the full-cell QV and dV/dQ curves are generated from a set of half-cell model parameters. This reconstruction is algebraic and does not require time-domain electrochemical simulation, so a complete fit is obtained in 2.74 ± 0.06 s for NSGA-II with three objectives and 9.04 ± 0.24 s for NSGA-III with four objectives on a single CPU core (Apple Silicon M1 Pro with 16 GB integrated memory) for the settings used in this work.

In practice, the method is not intended to run continuously in real time. Instead, it is used when a diagnostic dataset is available (e.g., a low-rate cycle). The identified degradation parameters are then stored and used for subsequent operation (see Fig. 14). This leads to three deployment scenarios:

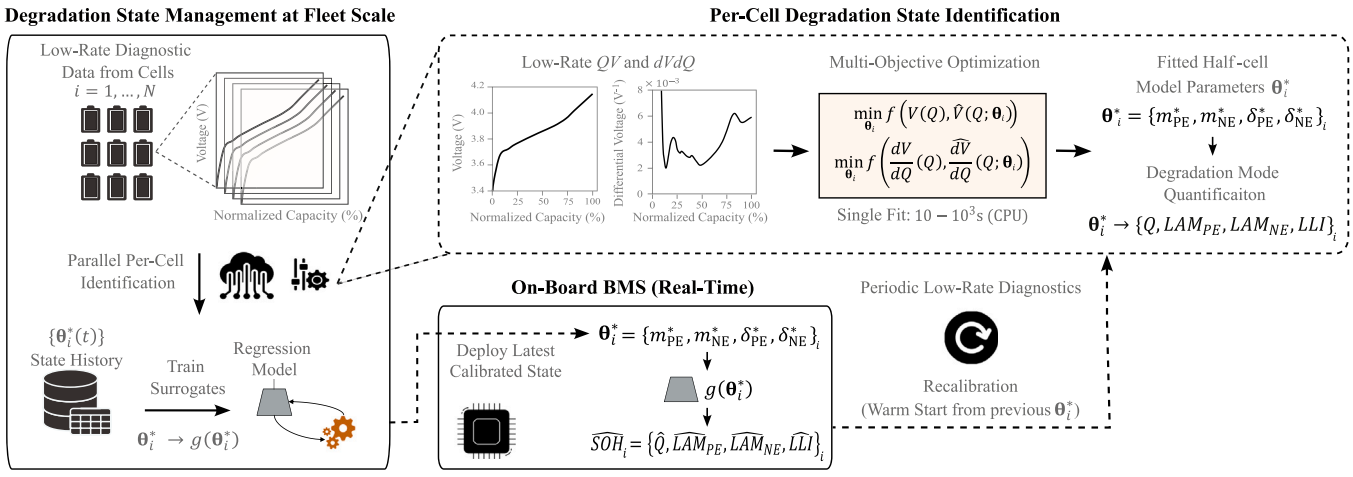

Fig. 14. Practical deployment workflow for fleet-scale degradation state management. Low-rate diagnostic data from cells $i = 1, \ldots, N$ are processed intermittently to identify the half-cell model parameter set θ_i^* via multi-objective optimization of the QV and dV/dQ responses. The fitted parameters are used to quantify the degradation modes, yielding component-level SOH metrics. For fleet deployment, parameter estimation for multiple cells can be performed independently and thus parallelized across cloud compute instances, while the resulting degradation states are stored as a time history $\{\theta_i^*(t)\}$. For on-board use, the optimizer is not executed in the BMS; instead, the latest calibrated state θ_i^* is deployed and evaluated in real time. To further reduce runtime, the forward evaluation can be replaced by a set of cell-specific surrogate models $g_i(\cdot)$ trained offline using synthetic data generated from the half-cell model or historical states data from the fitted cells, enabling fast embedded inference between periodic diagnostic recalibration events.

- **Offline analysis.** The full optimization is performed once per diagnostic dataset to obtain the degradation parameters and the reconstructed pOCV curve. In this case, the runtime is much shorter than the experimental acquisition time.
- **Cloud-based fleet diagnostics.** Each cell is processed independently, so the fitting can be parallelized across many compute instances. The method, therefore, scales linearly with the number of cells and can be applied to large fleets without modification.
- **On-board use.** The optimizer itself is not run in the BMS. Instead, the most recent set of degradation parameters is used for real-time SOH evaluation by directly reconstructing the voltage response. When a new diagnostic cycle becomes available, the optimization is rerun and initialized from the previous solution, reducing the number of required generations because the parameters change gradually with aging.

The runtime can be reduced further by replacing the forward reconstruction with a surrogate model. Following the physics-informed strategy proposed by Thelen et al. and Navidi et al. [27,29], the half-cell model can be used offline to generate synthetic data covering the admissible range of stoichiometries, active masses, and lithium inventory. Also, synthetic data can be generated by introducing perturbations, such as Gaussian noise with varying magnitudes, to simulate measurement noise arising from data-collection limitations in the field. A regression model can then be trained to directly predict the degradation parameters from the voltage features. In this case, the expensive optimization is needed only for generating the training data, while the deployed algorithm requires only a fast surrogate evaluation.

This structure supports two modes of operation. When applied to an individual diagnostic dataset, the method provides component-level SOH estimation by identifying the degradation parameters. When the identified parameters are tracked over time and their evolution is modeled, the same framework enables SOH forecasting without re-running the full optimization at every time step.

Stability of fitting under higher C-rates. Conventional degradation diagnostics using half-cell model parameterization require low C-rates (C/20–C/50) to obtain pOCV measurements closer to the equilibrium OCV. However, in real-world applications, pOCV curves at extremely low C-rates may not always be available, especially for on-device diagnostic workflows. Instead, measurements at higher C-rates may be used, which will inevitably introduce more effects from thermodynamic kinetics and polarization into the terminal voltage measurements. The additional kinetic change will alter the location and intensity of phase change peaks on differential curves [37,38,63]. The distortion effects become more significant in cells that undergo greater degradation [53]. Higher C-rates during data collection also lead to greater lithium heterogeneity on the electrode during intercalation, which can also alter peak behavior.

To accommodate the change in dV/dQ behavior due to different cycling rates, it is important to obtain the half-cell QV curves under the same C-rates to better capture the changes in kinetics under the given C-rates. Also, some simulation tools, such as the 'alawa Toolbox [18], can be used to interpolate and visualize the effect of different C-rates on the dV/dQ curves, provided that a sufficient amount of data under various C-rate conditions is available. In response to lithium heterogeneity, some advanced half-cell models can be implemented to capture the effect of stoichiometric differences across different regions of the electrode, such as superpositions of multiple offset pOCV curves representing the stoichiometric differences [32], or by using a more sophisticated half-cell model that can parameterize the lithium heterogeneity [34]. Even in such cases, the multi-objective optimization framework presented in this study, at least for the optimization setups that consider only MSE_{end} and MSE_{QV} objectives, should remain effective and robust because the model identifiability concerns will be partially, if not fully, addressed by adopting high C-rate half-cell measurements or incorporating dedicated model parameters to capture the effect from kinetic changes and lithium heterogeneity. As a feasible alternative, the physics-informed approaches highlighted in the earlier discussion of practical deployment considerations can be applied, specifically adapting the training data from higher C-rates.

More recently, the research community has gained traction by investigating measurements that are stable at higher C-rates to replace electrochemical responses for quantifying degradation modes. Notably, Pistorio et al. [64] investigated using changes in cell thickness during charging to estimate six electrode parameters (the capacity, the stoichiometric indices associated with a full-cell at the fully discharged state, and stoichiometric indices associated with a full-cell at

the fully charged state for both electrodes, respectively) across three PE chemistries (LFP, LCO, and NMC). The parameter estimation results from mechanical measurements (thickness vs. capacity) are compared against those from low-rate electrochemical measurements (voltage vs. capacity). By benchmarking against different chemistries and the discharge rate during measurement, they conclude that electrode parameters can be accurately estimated from mechanical measurements taken at a discharge rate of 1C. However, one major drawback of this method is the requirement of dedicated instrumentation for accurate thickness measurements during charge/discharge. Also, measuring the thickness of widely used cylindrical cells is even more challenging, often requiring advanced imaging techniques (e.g., high-throughput CT scans). Nevertheless, the multi-objective optimization framework can be naturally adapted to thickness and differential expansion measurements. Intuitively, the MSE_{QV} and $MSE_{dV/dQ}$ are directly analogous to the overall fitting error of the thickness change curves and the differential expansion curves, respectively. Also, there are peaks on differential expansion curves that can be related to electrode phase changes, and the peak alignment objective MSE_{peaks} can be easily adapted based on peak characteristics (e.g., number, locations, and relative heights). This highlights the potential of applying the proposed multi-objective optimization framework for model parameter identifications beyond battery half-cell models.

5. Conclusion

In this work, we propose and benchmark a multi-objective optimization framework for fitting the half-cell model, which can be used as a non-intrusive method for Li-ion battery degradation diagnostics at the component level. Throughout the two major benchmarking studies and the additional parametric and comparative studies, we identify the benefits of utilizing multiple objectives to achieve better performance in fitting a half-cell model. Specifically, we found that incorporating additional objectives based on QV endpoints and dV/dQ peaks can significantly improve the fitting in the context of aligning with the observed electrochemical processes (e.g., phase changes in graphite, electrode stoichiometry). Additionally, based on observations from benchmarking studies, we consolidate the general best practices and suggestions for fitting half-cell models via multi-objective optimization, streamlining the implementation for researchers and practitioners in the field.

There are still some limitations of this work that can be addressed by future research. The half-cell model is just one simplified empirical model for Li-ion batteries and cannot, in any way, capture all electrochemical or electromechanical behaviors in a cell throughout its aging. To tackle the challenge of no ground truth for quantifying degradation modes, one direction would be using other non-intrusive analytical techniques (e.g., CT scanning, electrochemical impedance spectroscopy) or additional diagnostic signals, such as current pulses, to provide additional insights into the degradation modes, and coupling with the half-cell model fitting approach to deliver a more robust estimation of each degradation mode. Also, data from other techniques can be used to cross-verify the degradation mode estimation obtained through the half-cell model.

CRediT authorship contribution statement

Tingkai Li: Writing – review & editing, Writing – original draft, Visualization, Software, Methodology, Investigation, Formal analysis, Conceptualization. **Yifan Zhang:** Writing – review & editing, Writing – original draft, Visualization, Software, Methodology, Investigation, Formal analysis. **Benjamin Nowacki:** Writing – review & editing, Writing – original draft, Visualization, Software, Formal analysis. **Sina Navidi:** Writing – review & editing, Software, Methodology, Investigation, Formal analysis. **Thomas Schmitt:** Writing – review & editing, Methodology, Investigation. **Shan Hu:** Writing – review & editing, Supervision, Project administration, Methodology, Investigation, Funding acquisition. **Chao Hu:** Writing – review & editing, Supervision, Project administration, Methodology, Investigation, Funding acquisition, Conceptualization.

Declaration of competing interest

The authors declare the following financial interests/personal relationships which may be considered as potential competing interests: Benjamin Nowacki is a co-founder and CEO of AmpWell, LLC. Chao Hu is a co-founder and CTO of AmpWell, LLC.

Acknowledgments

This work was supported in part by the US National Science Foundation under Grant ECCS-2015710. Any opinions, findings, or conclusions in this paper are those of the authors and do not necessarily reflect the sponsor's views. The authors would also like to thank Dr. Gaurav Jain and Dr. Hui Ye at Medtronic for providing the implantable-grade lithium-ion battery cells used to collect the cycling data used in this benchmarking study.

Appendix

A.1. Half-cell fabrication process and data acquisition

For the intent of this work, the term *half-cell* refers to an electrochemical cell consisting of a punched-out electrode sample from an electrochemically active full-cell paired with a lithium metal foil, which serves as the counter electrode [65]. The half-cell working electrode is either the positive electrode or the negative electrode from the full-cell. Typical cell chemistries use lithium cobalt oxide (LCO), lithium nickel cobalt aluminum oxide (NCA), lithium nickel manganese cobalt oxide (NMC), or lithium iron phosphate (LFP) as the active material of the positive electrode, with graphite serving as the active material of the negative electrode [41]. The electrode material used in half-cell fabrication is collected from either a commercial or a lab-fabricated full-cell, which could be in the form factor of a cylindrical, pouch, or prismatic cell. For commercial cells, electrode samples are usually obtained from pristine cells to provide more reliable and repeatable results. Depending on the actual degradation mechanisms experienced, electrodes from aged cells may be more prone to additional degradation caused by handling during the destructive process (i.e., recovering electrodes from aged full-cells). Meanwhile, for lab-fabricated cells, the pristine electrode materials are accessible, which allows researchers to build half-cells without recovering materials by disassembling a full-cell. The process of fabricating coin cells from each half-cell working electrode is outlined in Procedure A1 and illustrated in Fig. A.1. Let the half-cell containing the graphite sample be denoted by NE, as in the negative electrode of the full-cell. Consequently, the half-cell containing the transition metal oxide sample is denoted by PE.

After fabrication, experimental half-cells will be put on battery cyclers to obtain capacity versus voltage profiles, which usually consist of constant-current-constant-voltage (CCCV) charging and discharging steps. Time-series data for current and voltage are required to be recorded during cycling, and other measurements, such as capacity, power, and energy, can be derived from the current and voltage data. The testing environment and the appropriate cycling rate depend on the intention of the experiment. Half-cells should be placed in a thermal chamber or a well-controlled room temperature environment to minimize the deviation of ambient temperature during cycling. For the objective of developing an accurate half-cell model, preferable cycling rates would include charging and discharging currents lower than C/30. To ensure stable cycling performance of newly fabricated half-cells, it is recommended that half-cells undergo two or three low-rate break-in cycles before conducting the intended experiment. The lower and upper

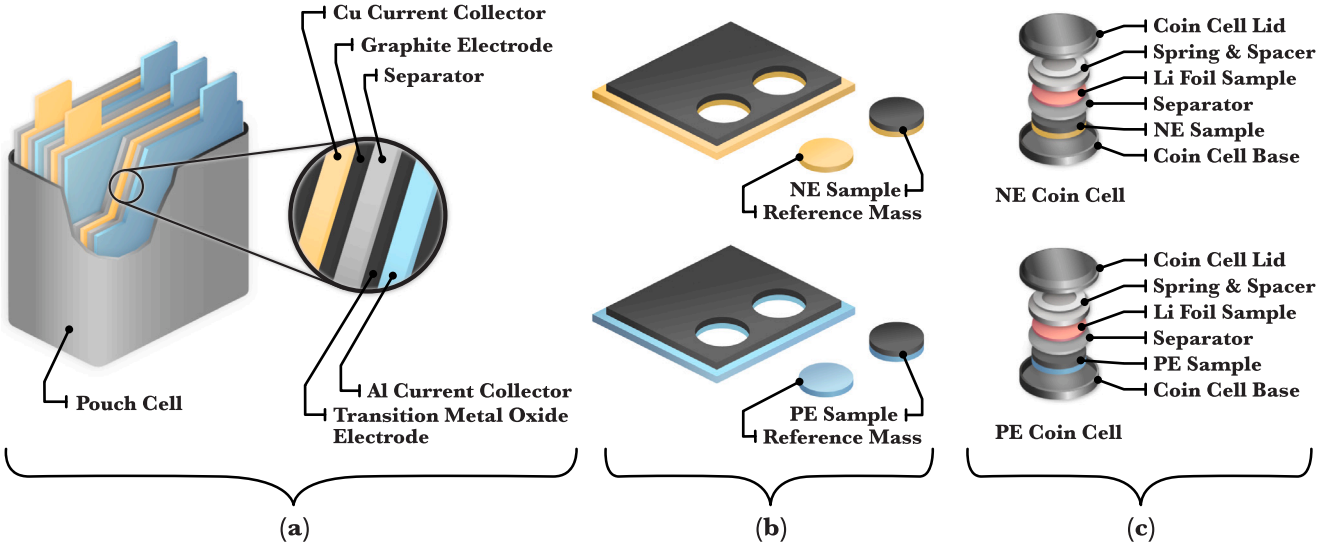

Fig. A.1. Illustration of the fabrication process for a half-cell, in coin cell form factor, created from a commercial pouch battery cell. (a) Typical layering of current collectors, electrodes, and separators inside a pouch cell. (b) Circular electrode samples and reference masses obtained from a single current collector layer. (c) Coin cell fabrication and layering from each electrode sample.

Procedure A1

Half-Cell Fabrication in Coin Cell Form Factor.

1	Inside an Argon environment, cut open the full-cell to reveal the stack (or roll) of single-cell layers. *This step is required only if using recovered electrodes for half-cell building.*
2	From each single-cell layer, separate the two current collectors. The copper current collector is coated with graphite active material. The transition metal oxide active material (dependent on the chosen cell chemistry) is coated on the aluminum current collector. *This step is required only if using recovered electrodes for half-cell building.*
3	Depending on the coin cell size required, take circular punches of a given diameter from each active material. The area of active material used (A_{PE} and A_{NE}) is thus determined by the punch size. See Figure S1 in the Supplementary Material for circular samples prepared for LFP/Gr experimental dataset described in Section 4.1. *Note that most commercial cells coat both sides of the current collectors with active material. For improved electronic conductivity between electrode samples and the coin cell base, and to prevent ionic transport disparities, remove the coating from one side of the collector before taking the electrode sample [65].*
4	Take additional samples of each current collector and strip all active material. These samples serve as the reference mass in calculating the active mass of each coin cell's working electrode.
5	Record the mass of each working electrode sample and subtract the corresponding reference current collector mass to obtain the active mass of each working electrode (m_{PE} and m_{NE}). *If the mass loading is known, Steps 4 and 5 can be skipped.*
6	From each working electrode sample, assemble a new coin cell using a lithium-foil counter electrode (formed with the same size circular punch). Place one of the working electrode samples into the coin cell base, followed by a glass microfiber separator. Wet the separator in a chosen electrolyte (preferably the same electrolyte and additives used in the full-cell) and place the lithium-foil sample on top. Place a spacer and spring washer on top of the working electrode and close the half-cell with the coin cell lid. Repeat this step for the other working electrode material. See Fig. A.1 for details on the coin cell layering and an overview of the fabrication process. *Note that the concentric alignment of the working electrode and lithium-foil samples is important. Alternatively, a slightly larger lithium foil sample can be used to avoid misalignment. The exact electrolyte composition used in commercial cells is often unknown, and the usage of a standard liquid electrolyte is acceptable. One of the typical electrolyte salts used in Li-ion cells is lithium hexafluorophosphate ($LiPF_6$), and examples of common solvents are ethylene carbonate (EC), diethyl carbonate (DEC), and dimethyl carbonate (DMC).*

voltage limits of half-cells depend on the material properties of each working electrode. For example, graphite half-cells are usually cycled between 0.01 V and 1.5 V, and LCO half-cells are cycled between 2.8 V and 4.3 V. Additionally, to fit a half-cell model, some full-cell voltage versus capacity data is needed, recorded at the same cycling rate as the half-cell potential curves. This avoids errors arising from mismatching cycling rates and is further discussed in the subsequent sections.

A.2. Discussion of the procedure, advantages, and disadvantages of manual half-cell model fitting

Manual half-cell model fitting is an expert-in-the-loop procedure for estimating the half-cell model parameters by iteratively adjusting parameters to obtain a physically plausible reconstruction of the full-cell QV curve and its diagnostic signatures (e.g., persistent dV/dQ peaks). In contrast to automatic fitting, which updates half-cell model parameters by minimizing predefined objective functions, manual fitting relies on a sequence of targeted edits guided by interpretability and visual agreement between measured and reconstructed curves.

In practice, the workflow begins by selecting an initial parameter set $\boldsymbol{\theta}_0$ (e.g., a chemistry-specific nominal guess, a baseline cell, or the fitted solution from the first RPT in the same aging trajectory). Using $\boldsymbol{\theta}_k$, the model generates a reconstructed curve $\hat{V}_{\text{cell}}(Q;\boldsymbol{\theta}_k)$ and the reconstruction is evaluated by overlaying QV curves and, when appropriate, dV/dQ. Parameters are then updated in a structured sequence, typically adjusting one component (or a small subset) at a time to preserve interpretability of each edit. First, mass/scaling terms (m_{PE}, m_{NE}) are tuned to match global capacity scaling and overall stretching/compression of the curve. Next, slippage terms (δ_{PE}, δ_{NE}) are adjusted to align major phase-transition features and correct horizontal offsets. After each update, the reconstruction is re-evaluated and checked against plausibility constraints, including feasible parameter bounds and (when fitting sequential RPTs for the same cell) preference for smooth parameter evolution and avoidance of implausible jumps. The procedure terminates when further edits yield marginal improvements and the fit meets the acceptance criteria used in this study (e.g., adequate QV agreement, endpoint consistency, and reasonable alignment of persistent diagnostic features).

Compared with automatic fitting, manual fitting can be advantageous when diagnostic features are unreliable or the loss landscape is misleading. For example, when dV/dQ is distorted by noise, peak

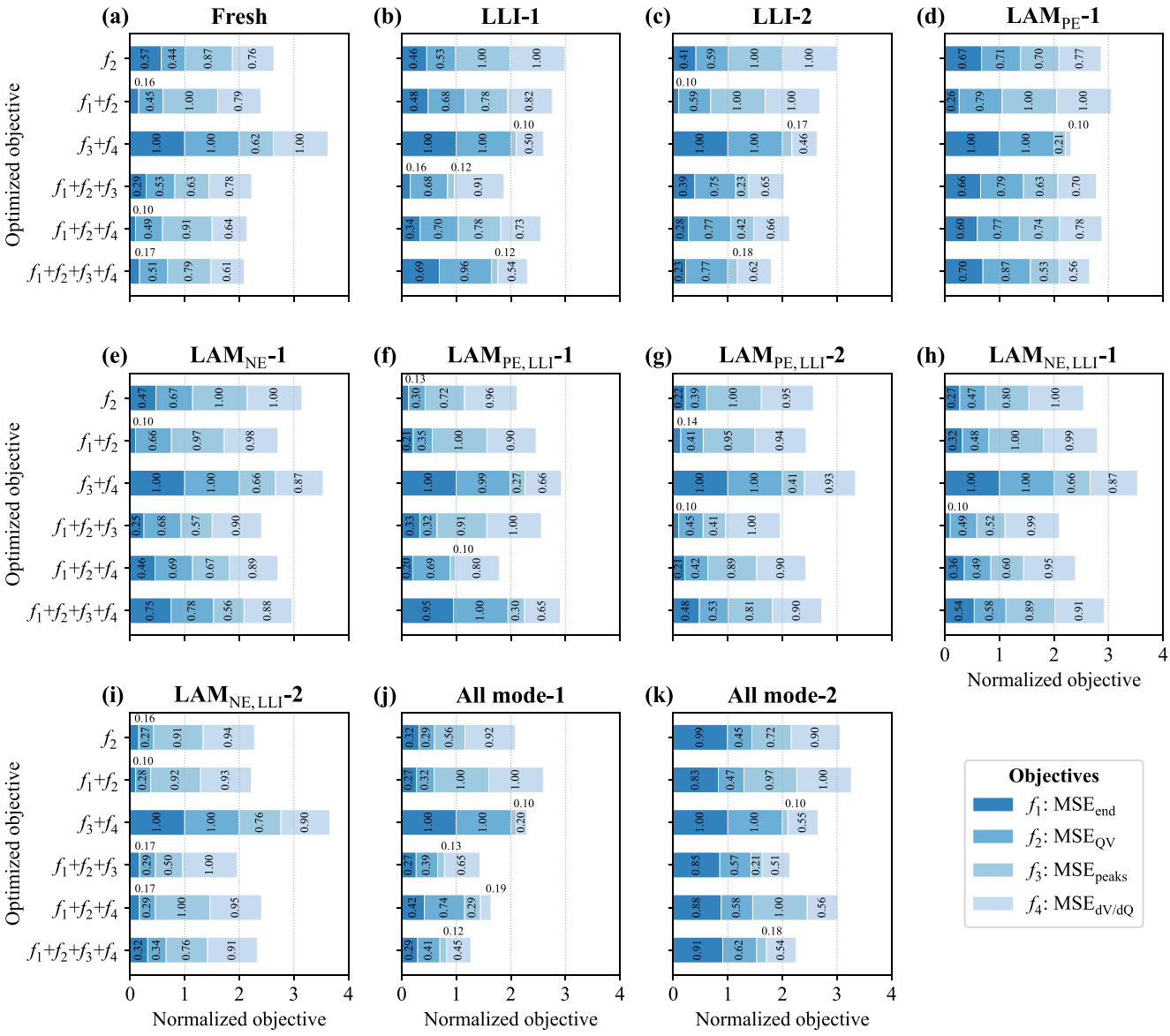

Fig. A.2. Comparisons of normalized objective values for six benchmarking cases on the LFP/Gr experimental emulation dataset (each objective is normalized to the interval [0.1, 1.0] to enhance readability).

splitting, discretization artifacts, or cell-to-cell variability, peak-based objectives can pull an optimizer toward non-physical solutions; manual fitting can selectively down-weight or ignore unreliable regions and emphasize robust QV structure and persistent signatures. Manual fitting can also provide better control over trajectory behavior across RPTs by explicitly enforcing continuity (and, where appropriate, chemistry-informed monotonicity), thereby reducing run-to-run variability and preventing implausible parameter discontinuities. Finally, manual fitting can prioritize interpretability-first solutions (e.g., stable alignment of phase-transition features) even when that slightly sacrifices a global error metric.

These benefits come with important drawbacks. Manual fitting is subjective and harder to reproduce because the edit sequence and stopping criteria depend on human judgment. It is also time-intensive and does not scale to large datasets or deployment settings where large numbers of curves must be processed consistently. Moreover, manual tuning can partially absorb unmodeled effects (e.g., temperature variation, rate dependence, or measurement artifacts) into $\boldsymbol{\theta}$, yielding visually good reconstructions that may not correspond uniquely to the underlying degradation mechanisms.

A.3. Additional panel plots for the benchmarking study on LFP/Gr experimental dataset

See Figs. A.2–A.4.

A.4. Additional panel plots for the benchmarking study on LCO/Gr aging dataset

See Figs. A.5–A.8.

Appendix B. Supplementary data

Supplementary material related to this article can be found online at https://doi.org/10.1016/j.etran.2026.100593.

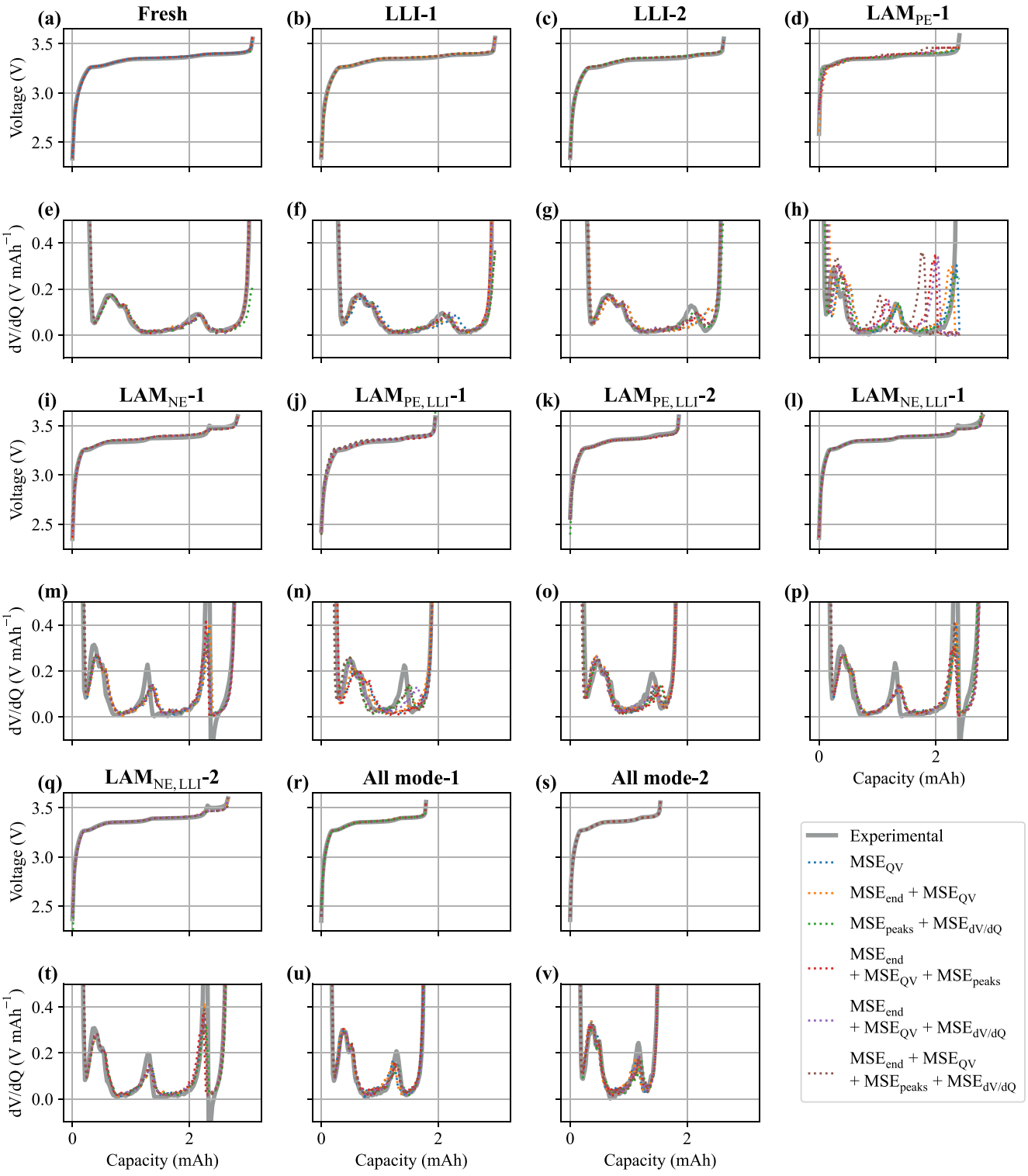

Fig. A.3. Comparison between the simulated QV and dV/dQ curves for all benchmarking cases on the LFP/Gr experimental emulation dataset.

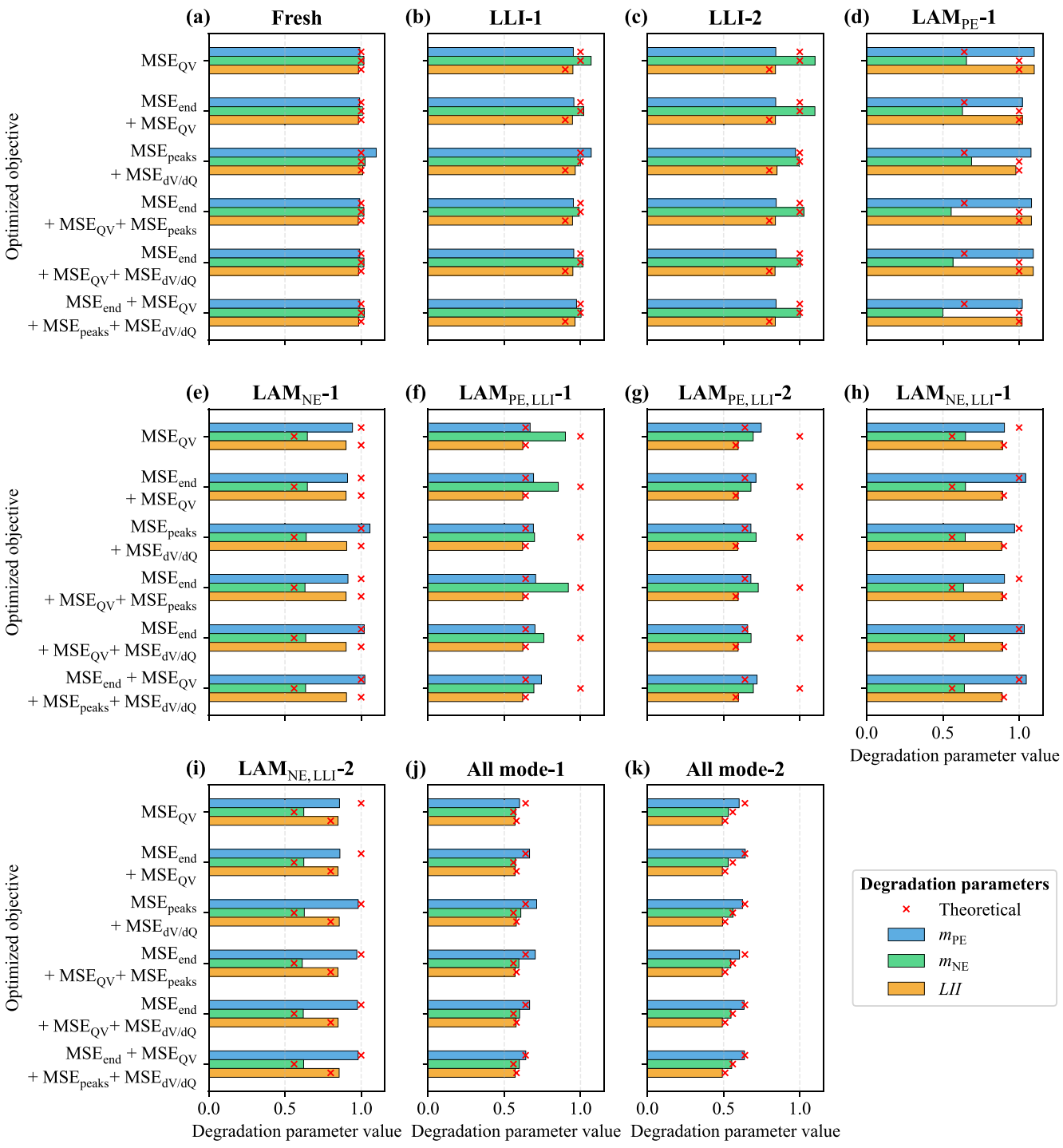

Fig. A.4. Comparison of estimated degradation parameters against the expected emulation for all six benchmarking cases on the LFP/Gr experimental emulation dataset.

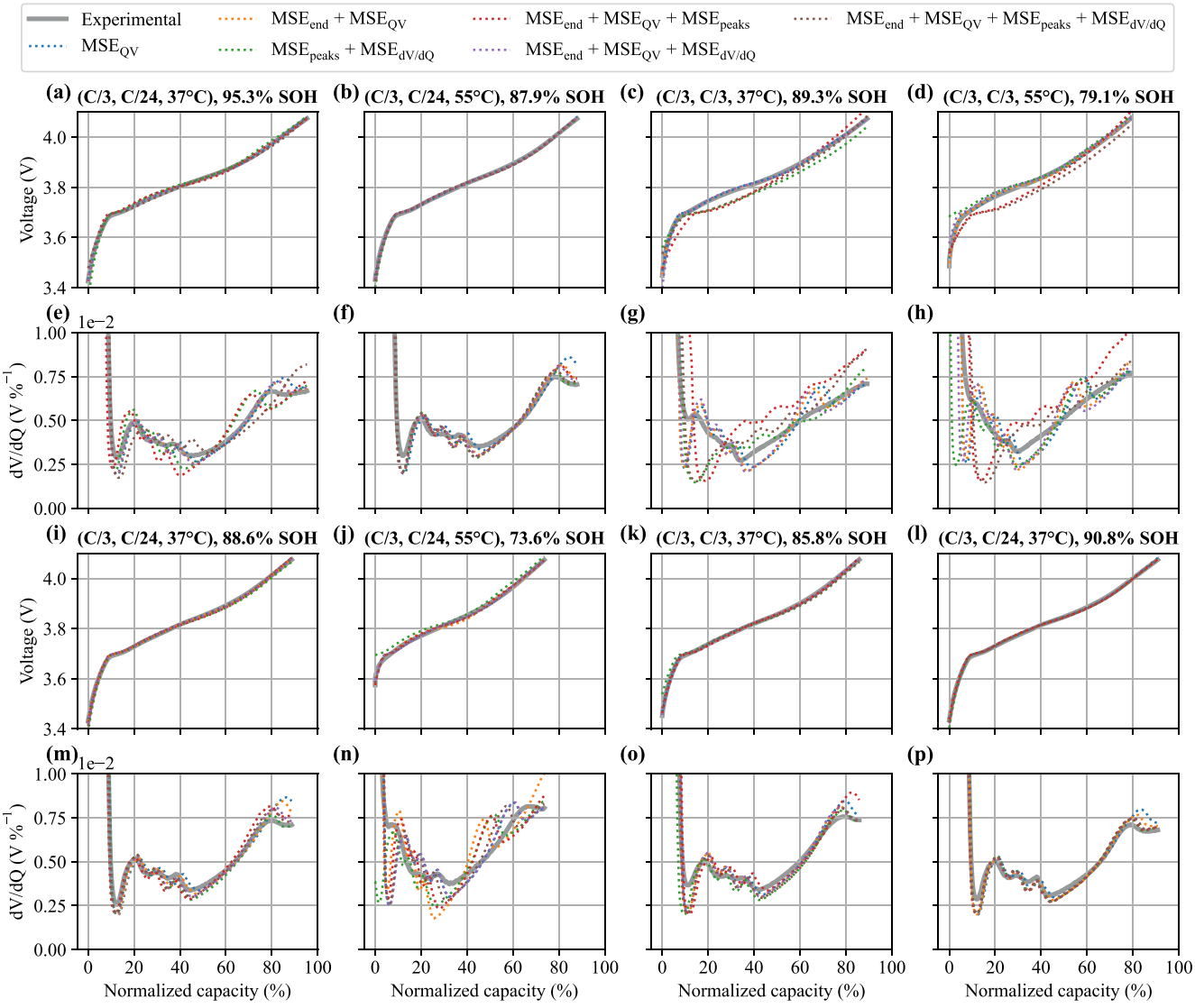

Fig. A.5. Comparison between the simulated QV and dV/dQ curves for all six benchmarking cases on the LCO/Gr cycling aging dataset.

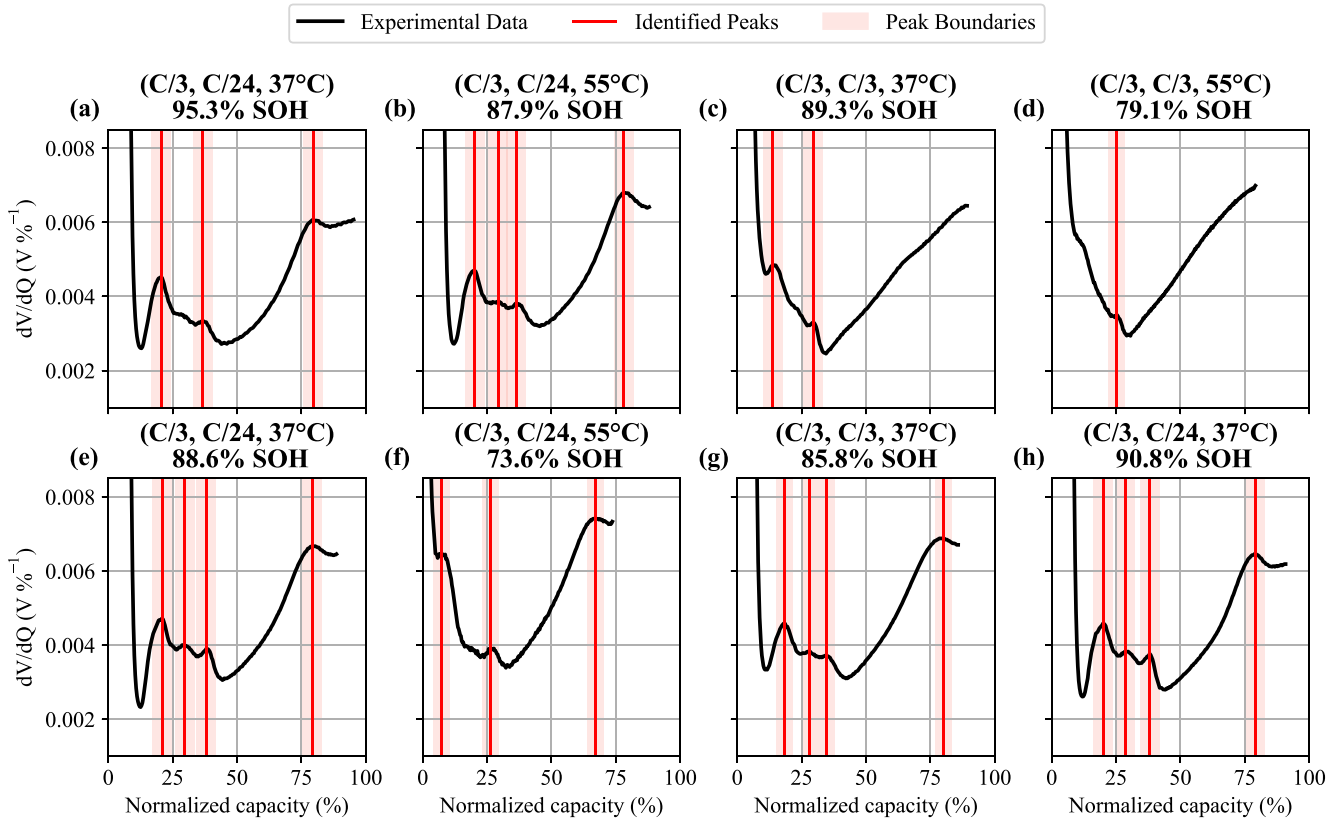

Fig. A.6. Identified peaks on dV/dQ curves of cells in the LCO/Gr cycling aging dataset.

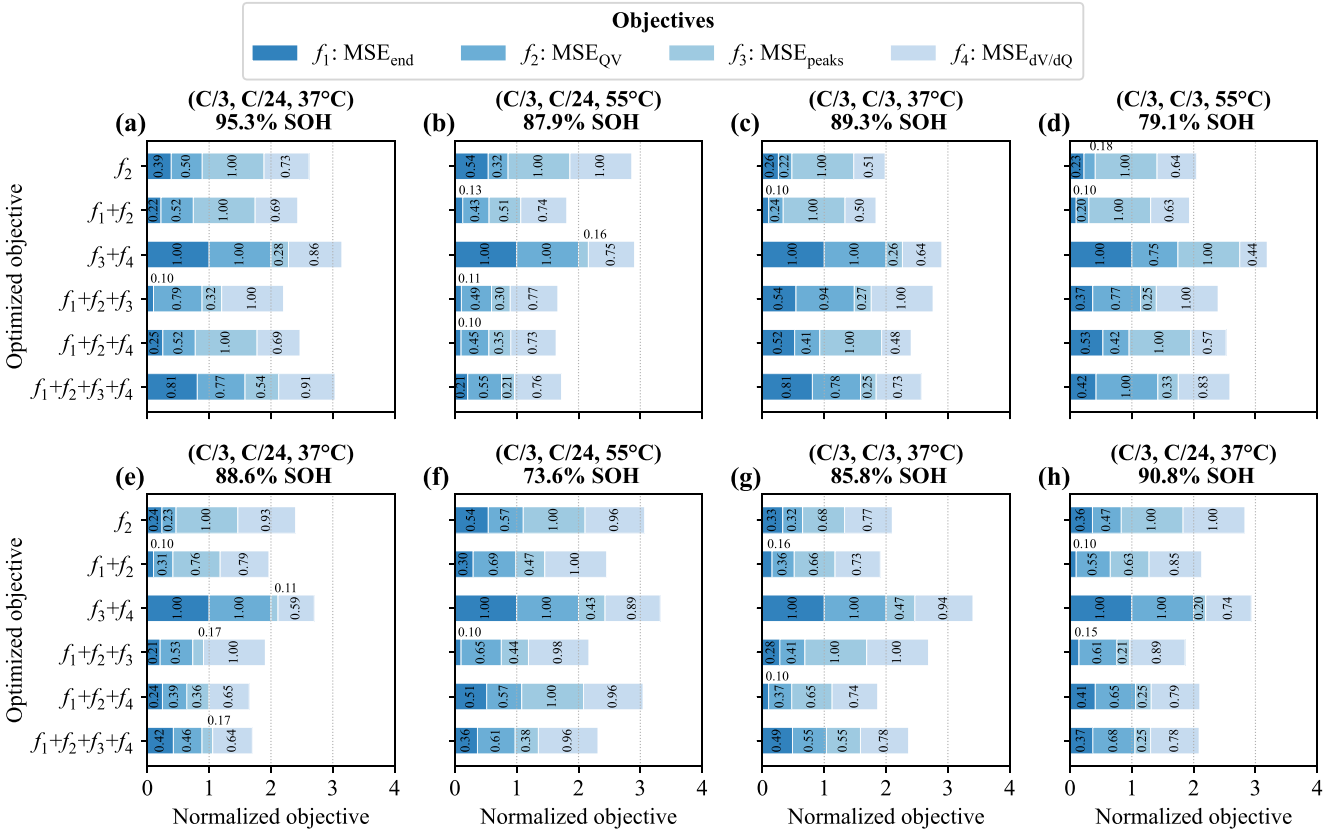

Fig. A.7. Comparison of normalized objective values for six benchmarking cases on the LCO/Gr cycling aging dataset (normalized with a value range [0.1, 1.0] for better visualization)

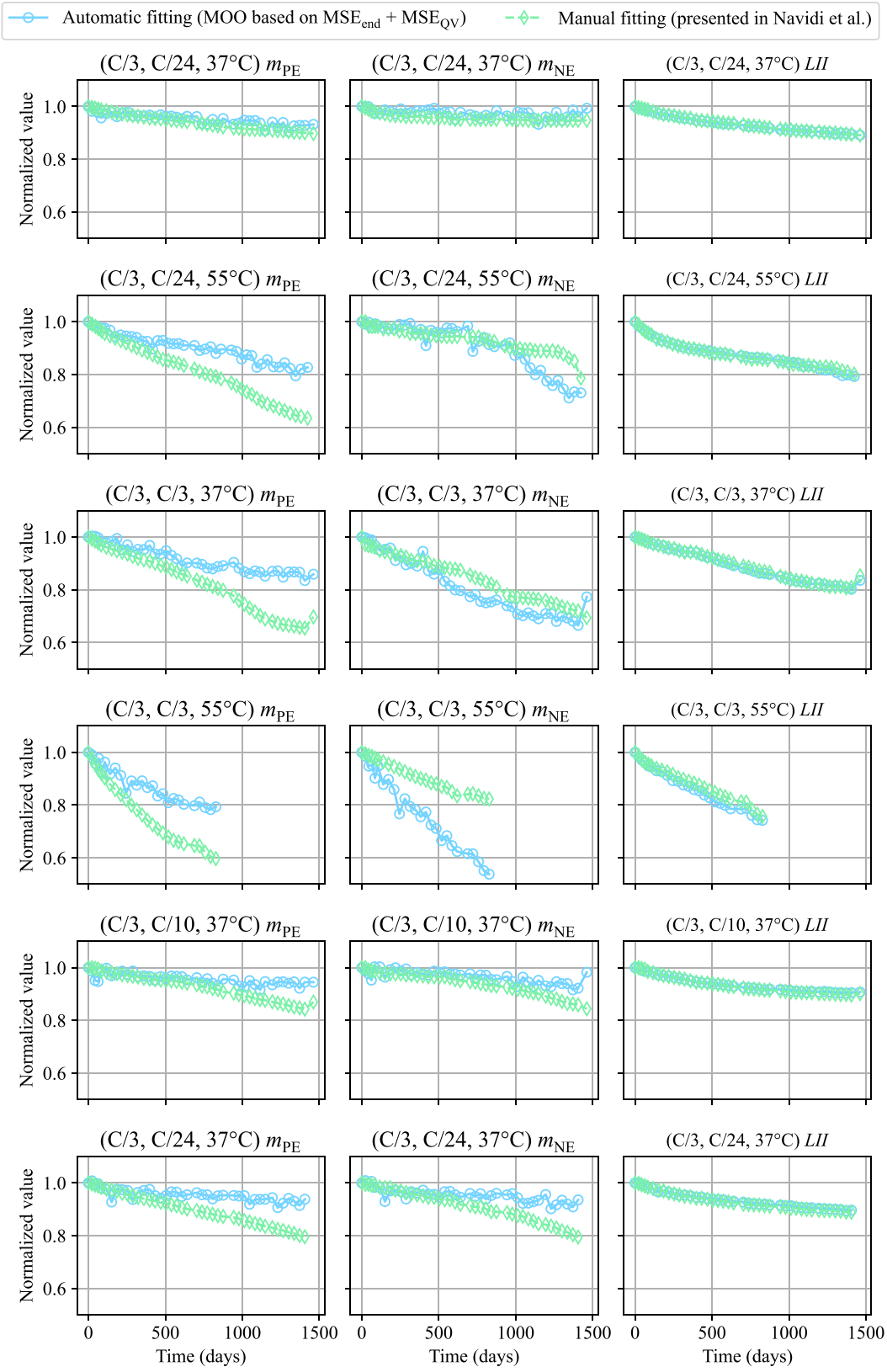

Fig. A.8. Comparisons of estimated degradation trajectories for six selected cells on the LCO/Gr cycling aging dataset.

Data availability

The ISU-UConn LFP/Graphite Emulated Degradation Dataset is available at https://digitalcommons.lib.uconn.edu/reil_datasets/6/. The code for data processing and degradation quantification is available on GitHub: https://github.com/REIL-UConn/Multi-Objective-Optimization-for-Lithium-Ion-Battery-Degradation-Diagnostics.

References

[1] Thelen Adam, Huan Xun, Paulson Noah, Onori Simona, Hu Zhen, Hu Chao. Probabilistic machine learning for battery health diagnostics and prognostics—review and perspectives. Npj Mater Sustain 2024;2(1):14. http://dx.doi.org/10.1038/s44296-024-00011-1.

[2] Li J, Adewuyi K, Lotfi N, Landers RG, Park J. A single particle model with chemical/mechanical degradation physics for lithium ion battery state of health (SOH) estimation. Appl Energy 2018;212:1178–90. http://dx.doi.org/10.1016/j.apenergy.2018.01.011.

[3] Bi Yalan, Yin Yilin, Choe Song-Yul. Online state of health and aging parameter estimation using a physics-based life model with a particle filter. J Power Sources 2020;476:228655. http://dx.doi.org/10.1016/j.jpowsour.2020.228655.

[4] Xu Zhicheng, Wang Jun, Lund Peter D, Zhang Yaoming. Co-estimating the state of charge and health of lithium batteries through combining a minimalist electrochemical model and an equivalent circuit model. Energy 2022;240:122815. http://dx.doi.org/10.1016/j.energy.2021.122815.

[5] Andersson Malin, Streb Moritz, Ko Jing Ying, Löfqvist Klass Verena, Klett Matilda, Ekström Henrik, Johansson Mikael, Lindbergh Göran. Parametrization of physics-based battery models from input–output data: A review of methodology and current research. J Power Sources 2022;521:230859. http://dx.doi.org/10.1016/j.jpowsour.2021.230859.

[6] Hu Chao, Youn Byeng D, Chung Jaesik. A multiscale framework with extended Kalman filter for lithium-ion battery SOC and capacity estimation. Appl Energy 2012;92:694–704. http://dx.doi.org/10.1016/j.apenergy.2011.08.002.

[7] Guha Arijit, Patra Amit. State of Health estimation of lithium-ion batteries using capacity fade and internal resistance growth models. IEEE Trans Transp Electrification 2018;4(1):135–46. http://dx.doi.org/10.1109/TTE.2017.2776558.

[8] Lin Chun-Pang, Cabrera Javier, Yang Fangfang, Ling Man-Ho, Tsui Kwok-Leung, Bae Suk-Joo. Battery state of health modeling and remaining useful life prediction through time series model. Appl Energy 2020;275:115338. http://dx.doi.org/10.1016/j.apenergy.2020.115338.

[9] Shen Sheng, Sadoughi Mohammadkazem, Li Meng, Wang Zhengdao, Hu Chao. Deep convolutional neural networks with ensemble learning and transfer learning for capacity estimation of lithium-ion batteries. Appl Energy 2020;260:114296. http://dx.doi.org/10.1016/j.apenergy.2019.114296.

[10] Li Weihan, Rentemeister Monika, Badeda Julia, Jöst Dominik, Schulte Dominik, Sauer Dirk Uwe. Digital twin for battery systems: Cloud battery management system with online state-of-charge and state-of-health estimation. J Energy Storage 2020;30:101557. http://dx.doi.org/10.1016/j.est.2020.101557.

[11] Roman Darius, Saxena Saurabh, Robu Valentin, Pecht Michael, Flynn David. Machine learning pipeline for battery state-of-health estimation. Nat Mach Intell 2021;3(5):447–56. http://dx.doi.org/10.1038/s42256-021-00312-3.

[12] Nowacki Benjamin, Ramamurthy Jayanth, Thelen Adam, Tischer Chad, Pint Cary L, Hu Chao. Rapid estimation of lithium-ion battery capacity and resistances from short duration current pulses. J Power Sources 2025;628:235813. http://dx.doi.org/10.1016/j.jpowsour.2024.235813.

[13] Nowacki Benjamin, Schmitt Thomas, Aquino Phillip, Hu Chao. Fine-tuning for rapid capacity estimation of lithium-ion batteries. Energy Storage Mater 2025;81:104425. http://dx.doi.org/10.1016/j.ensm.2025.104425.

[14] Liu Hongao, Li Chang, Hu Xiaosong, Li Jinwen, Zhang Kai, Xie Yang, Wu Ranglei, Song Ziyou. Multi-modal framework for battery state of health evaluation using open-source electric vehicle data. Nat Commun 2025;16(1):1137. http://dx.doi.org/10.1038/s41467-025-56485-7.

[15] Birkl Christoph R, Roberts Matthew R, McTurk Euan, Bruce Peter G, Howey David A. Degradation diagnostics for lithium ion cells. J Power Sources 2017;341:373–86. http://dx.doi.org/10.1016/j.jpowsour.2016.12.011.

[16] Wang Tiansi, Wang Hao, Shen Xiaoling, Lu Chenhao, Pei Lei, Xu Yixiang, Wang Wanlin, Li Huanhuan. Review of aging mechanism and diagnostic methods for lithium-ion batteries. Energies 2025;18(14):3884. http://dx.doi.org/10.3390/en18143884.

[17] Enrico De Santis, Vanessa Pennazzi, Massimiliano Luzi, Antonello Rizzi. Degradation mechanisms and differential curve modeling for non-invasive diagnostics of lithium cells: An overview. Renew Sustain Energy Rev 2025;211:115349. http://dx.doi.org/10.1016/j.rser.2025.115349.

[18] Dubarry Matthieu, Truchot Cyril, Liaw Bor Yann. Synthesize battery degradation modes via a diagnostic and prognostic model. J Power Sources 2012;219:204–16. http://dx.doi.org/10.1016/j.jpowsour.2012.07.016.

[19] Dubarry Matthieu, Anseán David. Best practices for incremental capacity analysis. Front Energy Res 2022;10:1023555. http://dx.doi.org/10.3389/fenrg.2022.1023555.

[20] Dubarry Matthieu, Berecibar M, Devie A, Anseán D, Omar N, Villarreal I. State of health battery estimator enabling degradation diagnosis: Model and algorithm description. J Power Sources 2017;360:59–69. http://dx.doi.org/10.1016/j.jpowsour.2017.05.121.

[21] Ansean David, Garcia Victor Manuel, Gonzalez Manuela, Blanco-Viejo Cecilio, Viera Juan Carlos, Pulido Yoana Fernandez, Sanchez Luciano. Lithium-ion battery degradation indicators via incremental capacity analysis. IEEE Trans Ind Appl 2019;55(3):2992–3002. http://dx.doi.org/10.1109/TIA.2019.2891213.

[22] Lui Yu Hui, Li Meng, Downey Austin, Shen Sheng, Nemani Venkat Pavan, Ye Hui, VanElzen Collette, Jain Gaurav, Hu Shan, Laflamme Simon, et al. Physics-based prognostics of implantable-grade lithium-ion battery for remaining useful life prediction. J Power Sources 2021;485:229327. http://dx.doi.org/10.1016/j.jpowsour.2020.229327.

[23] Li Tingkai, Zhou Zihao, Thelen Adam, Howey David A, Hu Chao. Predicting battery lifetime under varying usage conditions from early aging data. Cell Rep Phys Sci 2024;101891. http://dx.doi.org/10.1016/j.xcrp.2024.101891.

[24] Honkura Kohei, Honbo Hidetoshi, Koishikawa Yoshimasa, Horiba Tatsuo. State analysis of lithium-ion batteries using discharge curves. ECS Trans 2008;13(19):61–73. http://dx.doi.org/10.1149/1.3018750.

[25] Smith AJ, Dahn Hannah M, Burns JC, Dahn JR. Long-term low-rate cycling of $LiCoO_2$ /graphite Li-ion cells at 55°C. J Electrochem Soc 2012;159(6):A705–10. http://dx.doi.org/10.1149/2.056206jes.

[26] Birkl CR, McTurk E, Roberts MR, Bruce PG, Howey DA. A parametric open circuit voltage model for lithium ion batteries. J Electrochem Soc 2015;162(12):A2271. http://dx.doi.org/10.1149/2.0331512jes.

[27] Thelen Adam, Lui Yu Hui, Shen Sheng, Laflamme Simon, Hu Shan, Ye Hui, Hu Chao. Integrating physics-based modeling and machine learning for degradation diagnostics of lithium-ion batteries. Energy Storage Mater 2022;50:668–95. http://dx.doi.org/10.1016/j.ensm.2022.05.047.

[28] Navidi Sina, Thelen Adam, Li Tingkai, Hu Chao. Physics-informed neural networks for degradation diagnostics of lithium-ion batteries. In: Volume 3A: 49th design automation conference (DAC). Boston, Massachusetts, USA: American Society of Mechanical Engineers; 2023, http://dx.doi.org/10.1115/DETC2023-116940, V03AT03A049.

[29] Navidi Sina, Thelen Adam, Li Tingkai, Hu Chao. Physics-informed machine learning for battery degradation diagnostics: A comparison of state-of-the-art methods. Energy Storage Mater 2024;68:103343. http://dx.doi.org/10.1016/j.ensm.2024.103343.

[30] Zhu Chen, Sun Liqing, Chen Cheng, Tian Jinpeng, Shen Weixiang, Xiong Rui. Lithium-ion battery degradation diagnosis and state-of-health estimation with half cell electrode potential. Electrochim Acta 2023;459:142588. http://dx.doi.org/10.1016/j.electacta.2023.142588.

[31] Schmitt Julius, Schindler Markus, Oberbauer Andreas, Jossen Andreas. Determination of degradation modes of lithium-ion batteries considering aging-induced changes in the half-cell open-circuit potential curve of silicon–graphite. J Power Sources 2022;532:231296. http://dx.doi.org/10.1016/j.jpowsour.2022.231296.

[32] Fath Johannes Philipp, Dragicevic Daniel, Bittel Laura, Nuhic Adnan, Sieg Johannes, Hahn Severin, Alsheimer Lennart, Spier Bernd, Wetzel Thomas. Quantification of aging mechanisms and inhomogeneity in cycled lithium-ion cells by differential voltage analysis. J Energy Storage 2019;25:100813. http://dx.doi.org/10.1016/j.est.2019.100813.

[33] Hu Victor W, Schwartz Daniel T. Low error estimation of half-cell thermodynamic parameters from whole-cell li-ion battery experiments: Physics-based model formulation, experimental demonstration, and an open software tool. J Electrochem Soc 2022;169(3):030539. http://dx.doi.org/10.1149/1945-7111/ac5a1a.

[34] Kirst Cedric, Karger Alexander, Singer Jan P, Jossen Andreas. Non-destructive electrode potential and open-circuit voltage aging estimation for lithium-ion batteries. J Power Sources 2024;602:234341. http://dx.doi.org/10.1016/j.jpowsour.2024.234341.

[35] He Wei, Han Tao, Song Haiqin, Wang Qian, Kang Jianqiang, Wang Jing V, Chen Weihua. An extended single-particle model of lithium-ion batteries based on simplified solid-liquid diffusion process. IScience 2024;27(11):110764. http://dx.doi.org/10.1016/j.isci.2024.110764.

[36] Lee Suhak, Siegel Jason B, Stefanopoulou Anna G, Lee Jang-Woo, Lee Tae-Kyung. Electrode state of health estimation for lithium ion batteries considering half-cell potential change due to aging. J Electrochem Soc 2020;167(9):090531. http://dx.doi.org/10.1149/1945-7111/ab8c83, URL https://iopscience.iop.org/article/10.1149/1945-7111/ab8c83.

[37] Weng Andrew, Siegel Jason B, Stefanopoulou Anna. Differential voltage analysis for battery manufacturing process control. Front Energy Res 2023;11:1087269. http://dx.doi.org/10.3389/fenrg.2023.1087269.

[38] Mohtat Peyman, Lee Suhak, Sulzer Valentin, Siegel Jason B, Stefanopoulou Anna G. Differential expansion and voltage model for li-ion batteries at practical charging rates. J Electrochem Soc 2020;167(11):110561. http://dx.doi.org/10.1149/1945-7111/aba5d1.

[39] Sulzer Valentin, Marquis Scott G, Timms Robert, Robinson Martin, Chapman S Jon. Python Battery Mathematical Modelling (PyBaMM). J Open Res Softw 2021;9(1):14. http://dx.doi.org/10.5334/jors.309.

[40] Piruzjam Javid, Liu Guangming, Rubacek Lukas, Frey Marcus, Carraro Thomas. On the analytical solution of single particle models and semi-analytical solution of P2D model for lithium-ion batteries. Electrochim Acta 2024;492:144259. http://dx.doi.org/10.1016/j.electacta.2024.144259.

[41] Li Jianlin, Fleetwood James, Hawley W Blake, Kays William. From materials to cell: State-of-the-art and prospective technologies for lithium-ion battery electrode processing. Chem Rev 2022;122:903–56. http://dx.doi.org/10.1021/acs.chemrev.1c00565.

[42] Pei Lei, Wang Tiansi, Lu Rengui, Zhu Chunbo. Development of a voltage relaxation model for rapid open-circuit voltage prediction in lithium-ion batteries. J Power Sources 2014;253:412–8. http://dx.doi.org/10.1016/j.jpowsour.2013.12.083.

[43] Tian Jinpeng, Xiong Rui, Weixiang Shen Fengchun Sun. Electrode ageing estimation and open circuit voltage reconstruction for lithium ion batteries. Energy Storage Mater 2021;37:283–95. http://dx.doi.org/10.1016/j.ensm.2021.02.018.

[44] Jossen Andreas. Fundamentals of battery dynamics. J Power Sources 2006;154(2):530–8. http://dx.doi.org/10.1016/j.jpowsour.2005.10.041.

[45] Dubarry Matthieu, Beck David. Big data training data for artificial intelligence-based Li-ion diagnosis and prognosis. J Power Sources 2020;479:228806. http://dx.doi.org/10.1016/j.jpowsour.2020.228806.

[46] Dubarry Matthieu, Costa Nahuel, Matthews Dax. Data-driven direct diagnosis of Li-ion batteries connected to photovoltaics. Nat Commun 2023;14(1):3138. http://dx.doi.org/10.1038/s41467-023-38895-7.

[47] Kato Hisashi, Kobayashi Yo, Miyashiro Hajime. Differential voltage curve analysis of a lithium-ion battery during discharge. J Power Sources 2018;398:49–54. http://dx.doi.org/10.1016/j.jpowsour.2018.07.043.

[48] Deb K, Pratap A, Agarwal S, Meyarivan T. A fast and elitist multiobjective genetic algorithm: NSGA-II. IEEE Trans Evol Comput 2002;6(2):182–97. http://dx.doi.org/10.1109/4235.996017.

[49] Deb Kalyanmoy, Jain Himanshu. An evolutionary many-objective optimization algorithm using reference-point-based nondominated sorting approach, part I: Solving problems with box constraints. IEEE Trans Evol Comput 2014;18(4):577–601. http://dx.doi.org/10.1109/TEVC.2013.2281535.

[50] Seada Haitham, Deb Kalyanmoy. Non-dominated sorting based multi/many-objective Optimization: Two decades of research and application. In: Mandal Jyotsna K, Mukhopadhyay Somnath, Dutta Paramartha, editors. multi-objective optimization. Singapore: Springer Singapore; 2018, p. 1–24. http://dx.doi.org/10.1007/978-981-13-1471-1_1.

[51] Blank Julian, Deb Kalyanmoy. Pymoo: Multi-objective optimization in python. IEEE Access 2020;8:89497–509. http://dx.doi.org/10.1109/ACCESS.2020.2990567.

[52] Keil Peter, Jossen Andreas. Calendar Aging of NCA lithium-ion batteries investigated by differential voltage analysis and coulomb tracking. J Electrochem Soc 2017;164(1):A6066–74. http://dx.doi.org/10.1149/2.0091701jes.

[53] Clerici Davide, Pistorio Francesca, Somà Aurelio. Aging diagnostics in lithium-ion batteries with differential mechanical measurements. Appl Energy 2025;386:125524. http://dx.doi.org/10.1016/j.apenergy.2025.125524.

[54] Karimi Fariba, Lübke Mechthild, Wenzel Sebastian, Bobrowski Tim, Schmiegel Jan-Patrick, Kwade Arno. Degradation investigation of three Li-ion cell chemistries under different aging scenarios through differential voltage and post mortem analysis. J Power Sources 2024;618:235054. http://dx.doi.org/10.1016/j.jpowsour.2024.235054.

[55] Son Bongki, Ryou Myung-Hyun, Choi Jaecheol, Kim Sang-Hern, Ko Jang Myoun, Lee Yong Min. Effect of cathode/anode area ratio on electrochemical performance of lithium-ion batteries. J Power Sources 2013;243:641–7. http://dx.doi.org/10.1016/j.jpowsour.2013.06.062.

[56] Kim Sunghyeon, Lee Dongkyu, Han Youkyeong, Kim Hyun Woo, Yoo Dong-Joo. Abnormal lithium plating in the electrode edges at low N/P ratios in lithium-ion batteries. J Power Sources 2024;601:234301. http://dx.doi.org/10.1016/j.jpowsour.2024.234301.

[57] Schälte Yannik, Klinger Emmanuel, Alamoudi Emad, Hasenauer Jan. pyABC: Efficient and robust easy-to-use approximate Bayesian computation. J Open Source Softw 2022;7(74):4304. http://dx.doi.org/10.21105/joss.04304.

[58] Turner Brandon M, Van Zandt Trisha. A tutorial on approximate Bayesian computation. J Math Psych 2012;56(2):69–85. http://dx.doi.org/10.1016/j.jmp.2012.02.005.

[59] Virtanen Pauli, Gommers Ralf, Oliphant Travis E, Haberland Matt, Reddy Tyler, Cournapeau David, Burovski Evgeni, Peterson Pearu, Weckesser Warren, Bright Jonathan, van der Walt Stéfan J, Brett Matthew, Wilson Joshua, Millman K Jarrod, Mayorov Nikolay, Nelson Andrew RJ, Jones Eric, Kern Robert, Larson Eric, Carey C J, Polat İlhan, Feng Yu, Moore Eric W, VanderPlas Jake, Laxalde Denis, Perktold Josef, Cimrman Robert, Henriksen Ian, Quintero EA, Harris Charles R, Archibald Anne M, Ribeiro Antônio H, Pedregosa Fabian, van Mulbregt Paul, SciPy 10 Contributors. SciPy 1.0: Fundamental algorithms for scientific computing in python. Nature Methods 2020;17:261–72. http://dx.doi.org/10.1038/s41592-019-0686-2.

[60] Olson Jarred Z, López Carmen M, Dickinson Edmund JF. Differential analysis of galvanostatic cycle data from li-ion batteries: interpretative insights and graphical heuristics. Chem Mater 2023;35(4):1487–513. http://dx.doi.org/10.1021/acs.chemmater.2c01976.

[61] Gao Yizhao, Sun Ziqiang, Zhang Dong, Shi Dapai, Zhang Xi. Determination of half-cell open-circuit potential curve of silicon-graphite in a physics-based model for lithium-ion batteries. Appl Energy 2023;349:121621. http://dx.doi.org/10.1016/j.apenergy.2023.121621.

[62] Ferrari Victoria C, Lee Sang Bok, Rubloff Gary W, Stewart David M. Interface diagnostics platform for thin-film solid-state batteries. Energy & Environ Sci 2025;18(4):1783–800. http://dx.doi.org/10.1039/D4EE03915G.

[63] Fernando Alexa, Dubarry Matthieu. Model-free emulation of the impact of kinetics and temperature on commercial Li-ion batteries. J Power Sources 2025;654:237796. http://dx.doi.org/10.1016/j.jpowsour.2025.237796.

[64] Pistorio Francesca, Clerici Davide, Somà Aurelio. Diagnostics methodology based on differential mechanical measurements for lithium-ion batteries. Appl Energy 2025;397:126156. http://dx.doi.org/10.1016/j.apenergy.2025.126156.

[65] Murray Vivian, Hall David S, Dahn JR. A guide to full coin cell making for academic researchers. J Electrochem Soc 2019;166(2):A329–33. http://dx.doi.org/10.1149/2.1171902jes.